# WTS-2 b: a hot Jupiter orbiting near its tidal destruction radius around a K dwarf

J. L. Birkby,[1]⋆ M. Cappetta,[2] P. Cruz,[3] J. Koppenhoefer,[2,4] O. Ivanyuk,[5]
A. J. Mustill,[6,7] S. T. Hodgkin,[8] D. J. Pinfield,[9] B. Sipőcz,[9] G. Kovács,[8] R. Saglia,[2,4]
Y. Pavlenko,[5,9] D. Barrado,[3] A. Bayo,[10,11] D. Campbell,[9] S. Catalan,[9,12] L. Fossati,[13]
M.-C. Gálvez-Ortiz,[14] M. Kenworthy,[1] J. Lillo-Box,[3] E. L. Martín,[14] D. Mislis,[8]
E. J. W. de Mooij,[15] S. V. Nefs,[1] I. A. G. Snellen,[1] H. Stoev,[3] J. Zendejas,[2]
C. del Burgo,[16] J. Barnes,[9] N. Goulding,[9] C. A. Haswell,[13] M. Kuznetsov,[5,16]
N. Lodieu,[17,18] F. Murgas,[17] E. Palle,[17,18] E. Solano,[3,19] P. Steele[2] and R. Tata[17,18]

[1]*Leiden Observatory, Leiden University, Niels Bohrweg 2, NL-2333 CA Leiden, the Netherlands*
[2]*Max-Planck-Institut für extraterrestrische Physik, Giessenbachstrasse, D-85741 Garching, Germany*
[3]*Depto. Astrofísica, Centro de Astrobiología (INTA-CSIC), ESAC Campus, PO Box 78, E-28691 Villanueva de la Cañada, Spain*
[4]*Universitatssternwarte, Scheinerstrasse 1, D-81679 Munchen, Germany*
[5]*Main Astronomical Observatory of Ukrainian Academy of Sciences, Golosiiv Woods, Kyiv-127, UA-03680, Ukraine*
[6]*Departamento de Física Teórica, Facultad de Ciencias, Universidad Autónoma de Madrid, Cantoblanco, E-28049 Madrid, Spain*
[7]*Lund Observatory, Department of Astronomy and Theoretical Physics, Lund University, Box 43, SE-221 00 Lund, Sweden*
[8]*Institute of Astronomy, University of Cambridge, Madingley Road, Cambridge CB3 0HA, UK*
[9]*Centre for Astrophysics Research, University of Hertfordshire, College Lane, Hatfield, Hertfordshire AL10 9AB, UK*
[10]*European Southern Observatory, Alonso de Córdova 3107, Vitacura, Santiago, Chile*
[11]*Max Planck Institut für Astronomie, Königstuhl 17, D-69117 Heidelberg, Germany*
[12]*Department of Physics, University of Warwick, Gibbet Hill Rd, Coventry CV4 7AL, UK*
[13]*Department of Physical Sciences, The Open University, Walton Hall, Milton Keynes MK7 6AA, UK*
[14]*Centro de Astrobiología (CSIC-INTA). Crta, Ajalvir km 4, E-28850 Torrejón de Ardoz, Madrid, Spain*
[15]*Department of Astronomy and Astrophysics, University of Toronto, 50 St. George Street, Toronto, ON M5S 3H4, Canada*
[16]*Instituto Nacional de Astrofísica, Óptica y Electrónica, Luis Enrique Erro 1, Sta. Ma. Tonantzintla, Puebla, Mexico*
[17]*Instituto de Astrofísica de Canarias, Calle Vía Láctea s/n, E-38200 La Laguna, Tenerife, Spain*
[18]*Departamento de Astrofísica, Universidad de La Laguna (ULL), E-38205 La Laguna, Tenerife, Spain*
[19]*Spanish Virtual Observatory Thematic Network, Spain*

## ABSTRACT

We report the discovery of WTS-2 b, an unusually close-in 1.02-d hot Jupiter ($M_P = 1.12M_J$, $R_P = 1.30R_J$) orbiting a K2V star, which has a possible gravitationally bound M-dwarf companion at 0.6 arcsec separation contributing ∼20 per cent of the total flux in the observed $J$-band light curve. The planet is only 1.5 times the separation from its host star at which it would be destroyed by Roche lobe overflow, and has a predicted remaining lifetime of just ∼40 Myr, assuming a tidal dissipation quality factor of $Q'_\star = 10^6$. $Q'_\star$ is a key factor in determining how frictional processes within a host star affect the orbital evolution of its companion giant planets, but it is currently poorly constrained by observations. We calculate that the orbital decay of WTS-2 b would correspond to a shift in its transit arrival time of $T_{\mathrm{shift}} \sim 17$ s after 15 yr assuming $Q'_\star = 10^6$. A shift less than this would place a direct observational constraint on the lower limit of $Q'_\star$ in this system. We also report a correction to the previously published expected $T_{\mathrm{shift}}$ for WASP-18 b, finding that $T_{\mathrm{shift}} = 356$ s after 10 yr for $Q'_\star = 10^6$, which is much larger than the estimated 28 s quoted in WASP-18 b discovery paper. We attempted to constrain $Q'_\star$ via a study of the entire population of known transiting

⋆E-mail: birkby@strw.leidenuniv.nl

hot Jupiters, but our results were inconclusive, requiring a more detailed treatment of transit survey sensitivities at long periods. We conclude that the most informative and straightforward constraints on $Q'_\star$ will be obtained by direct observational measurements of the shift in transit arrival times in individual hot Jupiter systems. We show that this is achievable across the mass spectrum of exoplanet host stars within a decade, and will directly probe the effects of stellar interior structure on tidal dissipation.

**Key words:** surveys – planets and satellites: detection – planets and satellites: dynamical evolution and stability – planets and satellites: fundamental parameters – planets and satellites: individual: WTS-2 b.

# 1 INTRODUCTION

The orbital period distribution of gas giants is a fundamental property of planetary systems and places constraints on their formation processes, migration mechanisms, and future evolution. The observed period distribution is not smooth. The majority of hot Jupiters, i.e. those with a semimajor axis $a < 0.1$ au, are found in a 'pile-up' at periods of $P \sim 3$–4 d ($\sim$0.035–0.045 au), whereas only four hot Jupiters are found in very close-in orbits ($\lesssim$0.02 au, $\lesssim$1 d), namely WASP-18 b, WASP-43 b, WASP-19 b, and WASP-103 b (Hellier et al. 2009, 2011; Hebb et al. 2010; Gillon et al. 2014, respectively). The sharp decline of hot Jupiters in orbital periods less than two days is a genuine feature of the exoplanet period distribution, confirmed by both ground-based and space-based planet searches, e.g. *Kepler* (Howard et al. 2012) and SuperWASP (Hellier et al. 2012). This suggests that very close-in hot Jupiters are relatively rare, else current instrumentation would easily detect them on account of their very frequent and deep transits, and large radial velocity (RV) variations in comparison to longer period, smaller planets.

As a result, Hellier et al. (2011) argue that extreme systems like WASP-19 b are approximately one hundred times less common than those hot Jupiters in the pile-up, indicating that it is either difficult to get gas giants into very close orbits, or that they are quickly destroyed by strong tidal forces once they arrive. The latter would imply that very close-in hot Jupiters with old host stars are in the last few per cent of their lifetimes, which raises a further question of how likely it is to have observed these systems in a transient phase of their orbital evolution. Despite extensive theoretical work, our understanding of how tidal forces influence the orbital evolution of giant planets is poorly constrained by observation. The efficiency of the dissipation of the orbital energy due to frictional processes in the star is usually parametrized by a stellar tidal quality factor $Q'_\star$. Studies of binary star systems estimate its value to be $Q'_\star \sim 10^6$ (see e.g. Meibom & Mathieu 2005) and analysis of the tidal evolution of a small sample of exoplanets has found some evidence for consistency with this value ($10^6 < Q'_\star < 10^9$; Jackson, Greenberg & Barnes 2008). On the other hand, a recent exoplanet population study which tuned the value of $Q'_\star$ until the distribution of remaining planet lifetimes was statistically likely, found $Q'_\star \gtrsim 10^7$ at the 99 per cent confidence level (Penev et al. 2012) for its specific set of initial conditions. However, direct observational measurements of $Q'_\star$ in individual systems, i.e. the observation of a decaying orbital period, do not currently exist. $Q'_\star$ is the dominant factor in setting the pace of the orbital evolution for very close-in hot Jupiters and the unusually short predicted remaining lifetimes for planets such as WASP-18 b and WASP-19 b have led to a number of suggested modifications to the theory of stellar tides that reduce the efficiency of the dissipation. For example, Winn et al. (2010) speculate that

the observed increase in misalignment between the planetary orbit and stellar spin axes for hot Jupiters orbiting hotter stars depends on the depth of the convective zone in the host star. Here, cooler stars with deeper convective envelopes dissipate the orbital energy more efficiently resulting in a faster alignment of the stellar obliquity, in keeping with theoretical studies (e.g. Barker & Ogilvie 2009, 2010; Penev & Sasselov 2011). Others suggest that there is a complicated dependency on the planetary mean motion that results in zones of inefficient tidal dissipation during inspiral (Ogilvie & Lin 2007), or even possible mass-loss effects that act to slow the orbital evolution of the planet (Li et al. 2010).

In this paper, we present the discovery and characterization of the hot Jupiter WTS-2 b. It is the second planet to be detected in the infrared light curves of the WFCAM Transit Survey (WTS; Cappetta et al. 2012; Kovács et al. 2013), and orbits a mid-K dwarf star at just 1.5 times the separation at which it would be destroyed by tidal forces, making it a useful benchmark in constraining the theory of stellar tides. The remainder of this paper is organized as follows: in Section 2, we briefly summarize the goals of the WTS and its atypical observing strategy, the reduction procedure used to generate the infrared light curves, and the processes used to identify WTS-2 b as a transiting candidate and the checks performed before proceeding with its follow-up observations. Section 3 describes all of the follow-up data we obtained for WTS-2 b and their data reduction. We characterize the WTS-2 host star in Section 4, and derive the corresponding properties of its planetary companion WTS-2 b in Section 5. Section 6 summarizes our investigation into possible blending scenarios. In Section 7, we calculate and discuss the tidal evolution and remaining lifetime of WTS-2 b. We calculate the expected shift in its transit arrival time after 10 yr, assuming that its orbit is decaying under tidal forces with $Q'_\star = 10^6$, and we give a correction to the previously published expected shift in the transit arrival time for WASP-18 b in Section 7.2.1. In Section 7.3, we also attempt to constrain $Q'_\star$ using the known population of hot Jupiters. Finally, we assess the potential for characterizing the atmosphere of WTS-2 b using ground-based telescopes in Section 7.4. Our conclusions are summarized in Section 8.

## 2 THE WFCAM TRANSIT SURVEY

The WTS is a photometric monitoring campaign that covered $\sim$6 sq. degrees of the sky. It used the 3.8 m United Kingdom Infrared Telescope (UKIRT) on Mauna Kea, Hawaii, in conjunction with the Wide-Field Camera (WFCAM), to observe at infrared wavelengths (*J* band, 1.25 μm). The survey began on 2007 August 5. A detailed description of the WTS and its goals can be found in Kovács et al. (2013), Birkby et al. (2012), and Zendejas et al. (2013), but its main features are recounted here briefly for reference. The WTS light curves were observed at infrared wavelengths
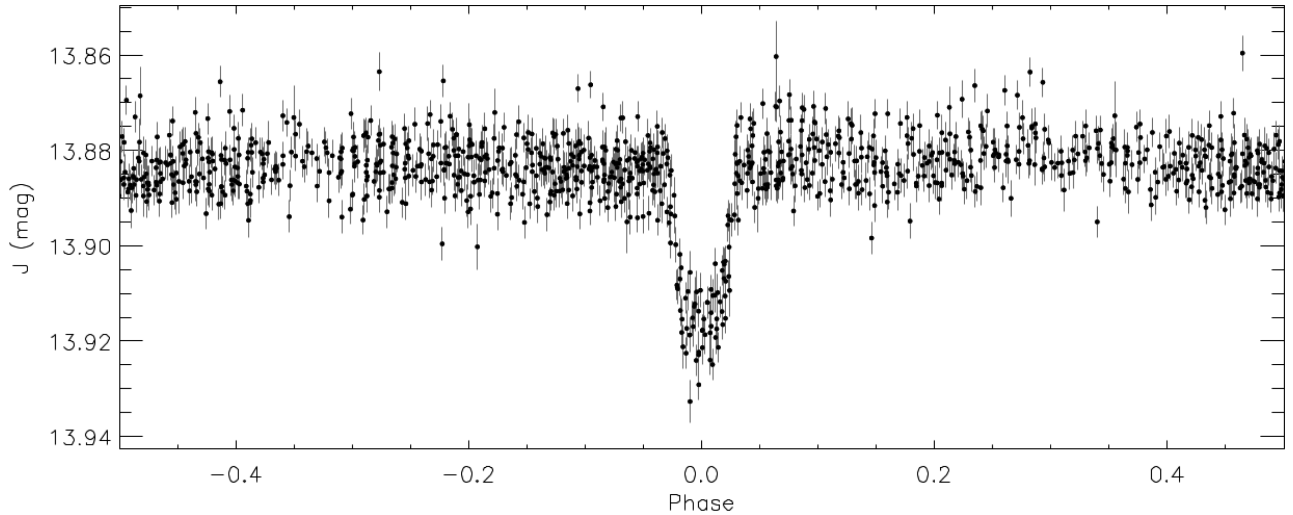
**Figure 1.** The full phase-folded discovery light curve of WTS-2 b from WTS *J*-band observations. The data are not binned. The out-of-eclipse rms is 5.3 mmag. The data for this figure are given in Table 1. Note that this light curve has not been corrected for dilution by the additional faint light source also within the aperture (see Section 3.5).

in order to maximize sensitivity to photons from M dwarfs. However, for the earlier type stars in the WTS fields, infrared observations have the added advantage of being less sensitive to low-level star spot modulation, thus providing more stable light curves in which to hunt for planets (Goulding et al. 2012). The WTS covered four fields distributed in RA so that at least one field was always visible within 15° of zenith from Mauna Kea. This was key to the survey's observing strategy as it operated as a back-up programme in the highly efficiently queue-scheduled operational mode of UKIRT, observing in sky conditions that the UKIRT large programmes, such as UKIRT Infrared Deep Sky Survey (UKIDSS; Lawrence et al. 2007), could not use. Consequently, the majority of the WTS observations are taken in the first hour of the night when the atmosphere was still cooling and settling; however, the back-up nature of the programme served to randomize the observing pattern. The exact field locations were chosen to minimize giant contamination, while maximizing the number of early M dwarfs and maintaining $E(B - V) < 0.1$ mag, which kept the fields at $b > 5°$. WTS-2 b was found in the '19 h field', which is centred at RA = $19^h$, Dec. = $+36^d$ and contains $\sim$65 000 stellar sources at $J \leq 17$ mag. Note that this field is very close to, but does not overlap with the *Kepler* field of view (Batalha et al. 2006), which has been shown to have a low fraction of late-K and early M giants at optical magnitudes comparable to the WTS (Mann et al. 2012).

### 2.1 Observation and reduction of the UKIRT/WFCAM *J*-band time series photometry

The infrared light curves of the WTS were generated from time series photometry taken with the WFCAM imager (Casali et al. 2007) mounted at the prime focus of UKIRT. WFCAM consists of four 2048 × 2048 18 µm pixel HgCdTe Rockwell Hawaii-II, non-buttable, infrared arrays. The arrays each cover 13.65 arcmin × 13.65 arcmin (0.4 arcsec pixel$^{-1}$) and are arranged in a square paw-print pattern, separated by 94 per cent of an array width. The four WTS field cover 1.5 sq. degree each, which requires eight pointings of the WFCAM paw print, tiled together to give uniform coverage. The WTS observed a 9-point jitter pattern of 10 s exposures at each pointing, resulting in a cadence of one data point per 15 min in any given 1 h observing block (9 × 10 s × 8 + overheads).

The 2D image processing of the WFCAM images and the generation of the WTS light curves is described in detail by Kovács et al. (2013) and closely follows the methods of Irwin et al. (2007). In summary, we remove the dark current and reset anomaly from the raw images, apply a flat-field correction using twilight flats, then decurtain and sky subtract. Astrometric and photometric calibration was achieved using Two Micron All Sky Survey (2MASS) stars in the field of view (Hodgkin et al. 2009). To generate the light curves, we made a master catalogue of source positions using a stacked image of the 20 best frames and used it to perform list-driven, colo-cated, variable aperture photometry. For WTS-2, the best aperture radius (i.e. the one that gave the smallest rms) was equal to $\sqrt{2}$ times the typical full width at half-maximum (FWHM) of the stellar images across all frames, i.e. 3.5 pixels (1.98 arcsec). In an attempt to remove systematic trends in the light curves, e.g. those caused by flat-fielding inaccuracies or varying differential atmospheric extinction across the wide field of view, we fit a 2D quadratic polynomial to the flux residuals in each light curve as a function of the source position on the detector. This step can significantly reduce the rms of the brightest objects in wide-field surveys (Irwin et al. 2007). Finally, we removed residual seeing-correlated effects by fitting a quadratic polynomial to the flux residuals in each light curve as a function of the stellar image FWHM on the corresponding frame.

The resulting *J*-band light curves for the 19 h field have a median rms of $\sim$1 per cent ($\sim$10 mmag) or better for $J \leq 16$ mag, with a per data point precision of $\sim$3−5 mmag for the brightest targets (saturation occurs at $J \sim 13$ mag).[1] The out-of-eclipse data in the light curve of WTS-2 ($J_{WFCAM} = 13.88$ mag) has a per data point precision of 5.3 mmag. The full, phase-folded, unbinned *J*-band light curve of WTS-2 b is shown in Fig. 1, and the data are given in Table 1.

### 2.2 Detection and prioritization of WTS transit candidates

The vast sample of stars in the WTS and its randomized observing strategy do not permit a straightforward eyeball search for

---

[1] The rms is calculated using the robust median of absolute deviations (MAD) estimator, scaled to the equivalent Gaussian standard deviation (i.e. rms $\sim 1.48 \times$MAD).

**Table 1.** The observed WFCAM *J*-band light curve data for WTS-2 b without correction for dilution. Magnitudes are given in the WFCAM system. Hodgkin et al. (2009) provide conversions for other systems. The errors, $\sigma_J$, are estimated using a standard noise model, including contributions from Poisson noise within the object aperture, sky noise, readout noise, and errors in the sky background estimation. (This table is published in full in the online paper and is shown partially here for guidance regarding its form and content.)

| HJD | $J_{\mathrm{WFCAM}}$ (mag) | $\sigma J_{\mathrm{WFCAM}}$ (mag) |
|---|---|---|
| 245 4317.810 999 | 13.9219 | 0.0033 |
| 245 4317.823 059 | 13.9245 | 0.0032 |
| – | – | – |

transits in the light curves, so we undertook several steps to reduce the enormity of this task. All stellar sources in the 19 h field with $J < 17$ mag were first passed through the box-least-squares transit detection algorithm OCCFIT, which is described in detail by Aigrain & Irwin (2004). Like all ground-based transit surveys, the processed WTS light curves suffer from residual correlated red noise, which can mimic transit events. We therefore adjusted the detection significance statistic, $S$, calculated by OCCFIT to account for the presence of red noise following the model of Pont, Zucker & Queloz (2006) to give $S_{\mathrm{red}}$. In order to qualify as a WTS transit candidate, a detection must have $S_{\mathrm{red}} \geq 5$. We also rejected transit detections in the period range $0.99 < P < 1.005$ d, as the majority of these were found to be aliases caused by the observing window function of our ground-based survey.

In the final step before eyeballing the remaining light curves, we used *ZYJHK* single epoch photometry from WFCAM (see Section 3.1), plus complementary *griz* photometry from Sloan Digital Sky Survey data release 7 (SDSS DR7; York et al. 2000) to create a spectral energy distribution (SED) for each object and estimate its effective temperature (see Birkby et al. 2012 for details). The effective temperature, $T_{\mathrm{eff}}$, was converted to an approximate stellar radius for each source, using the stellar evolution models of Baraffe et al. (1998), at an age of 1 Gyr with a mixing length equal to the scale height. Assuming a maximum planetary radius of $2R_J$, we defined an envelope of transit depths as a function of stellar radius that were consistent with planetary transit events. Only detections with changes in flux ($\Delta F$) corresponding to $R_\star/\sqrt{(\Delta F)} \leq 2R_J$ were allowed through to the eyeballing stage. It is important to note firstly that OCCFIT tends to underestimate transit depths because it does not allow for the trapezoidal shape of a transit, nor does it account for limb-darkening effects. Secondly, the models we use to estimate the stellar radii systematically underestimate the temperature of solar-like stars (Baraffe et al. 1998), making our first estimates of $T_{\mathrm{eff}}$ too cool for stars of earlier type than M dwarfs and hence initial radius estimates that are too small. Both of these factors combined make it unlikely that genuine hot Jupiter transit events are rejected by this final selection criterion.

The ~3500 candidates that survived to the eyeball stage were mostly false positives arising from nights of bad data or singular bad frames that we do not filter from the data. We also removed binary systems that were detected on half of their true orbital period (as is favoured by the detection statistic). Overall, with this method we detected 40 good transiting candidates, including WTS-2 b, which has $S_{\mathrm{red}} = 23$, an OCCFIT-detected period of 1.0187 d, and initial estimated stellar effective temperature $T_{\mathrm{eff}} = 4777$ K, and an

OCCFIT-detected transit depth of $\Delta F = 0.031$, corresponding to an estimated planet radius of $\sqrt{0.031} \times 0.82\,\mathrm{R_\odot} \sim 1.4 R_J$.

Before proceeding with follow-up observations, we checked that the stellar density calculated from the phase-folded light curve of WTS-2 b matched the estimated stellar type from the initial SED model fit, using the method described by Seager & Mallén-Ornelas (2003). A large discrepancy would suggest a blended or grazing binary system. We found a light-curve stellar density of $\rho_\star \sim 1.49\rho_\odot$, which is within $\sim 0.05\rho_\odot$ of the model density for a 4777 K star at 1 Gyr in the Baraffe et al. (1998) models. The close agreement between the stellar densities from SED modelling and the phase-folded light curve triggered the follow-up observations to characterize WTS-2 b.

## 3 FOLLOW-UP OBSERVATIONS AND DATA REDUCTION

### 3.1 Multiwavelength single epoch broad-band photometry

In order to measure the photometric colours and estimate the spectral type of WTS-2 (and all the other sources in the WTS), we used WFCAM to observe single, deep exposures of the four WTS fields in five filters (*ZYJHK*), with exposure times 180, 90, 90, $4 \times 90$, and $4 \times 90$ s, respectively. The 2D image processing for these data are the same as described in Section 2.1. For WTS-2, we also obtained Johnson *B*-, *V*- and *R*-band single epoch photometry on the nights of 2012 March 8 and 22 at the University of Hertfordshire's Bayfordbury Observatory (latitude = 51°.8 north, longitude = 0°.1 west). We used a Meade LX200GPS 16-inch *f*/10 telescope fitted with an SBIG STL-6303E CCD camera, and integration times of 300 s per band. Images were bias, dark, and flat-field corrected, and the extracted aperture photometry was calibrated using three bright reference stars within the image. The quoted photometric uncertainties for this data combine the contribution from the signal-to-noise ratio (SNR) of the source (typically ~20) with the scatter in the zero-point from the calibration stars.

A further nine photometric data points at optical and infrared wavelengths were gathered for WTS-2 using the publicly available Virtual Observatory SED Analyzer[2] (VOSA; Bayo et al. 2008, 2013), including *ugriz* from the SDSS DR7 (York et al. 2000), *JHK* from the 2MASS (Skrutskie et al. 2006), and *W1W2* from the *Wide-field Infrared Survey Explorer* (*WISE*; Wright et al. 2010). We do not give the *W3* and *W4* bandpasses as they fall below the *WISE* $5\sigma$ point source sensitivity for detection. We also note that the *u* band for SDSS photometry is affected by a known red leak in the filter and has been assigned an accordingly larger error.[3] All of the available single epoch broad-band photometry for WTS-2 is reported in Table 2 and plotted in Fig. 2. The data are used in Section 4 to determine the best-fitting SED for WTS-2.

### 3.2 INT/WFC *i*-band time series photometry

In order to confirm the transit of WTS-2 b and to help constrain the transit model, on 2010 July 18 we obtained further time series photometry in the Sloan *i* band using the Wide Field Camera (WFC) on the 2.5 m Isaac Newton Telescope (INT) at Roque de Los Muchachos, La Palma. A total of 67 frames covering the full transit with some out-of-transit baseline were obtained with exposures times of 90 s, at a cadence of 1 data point every 2.45 min (the overheads include the CCD readout time plus time allowed for the

---

[2] http://svo2.cab.inta-csic.es/svo/theory/vosa
[3] See http://www.sdss3.org/dr8/imaging/caveats.php

**Table 2.** Broadband photometry for WTS-2. All reported magnitudes are in the Vega system except the SDSS photometry, which is in the AB magnitude system. These magnitudes have not been corrected for reddening, nor for the dilution by the faint red source within 0.6 arcsec of the host star (see Section 3.5). $\lambda_{eff}$ is the effective wavelength defined as the mean wavelength weighted by the transmission function of the filter, and EW is the equivalent width of the bandpass.

| Filter | $\lambda_{eff}$ (Å) | EW (Å) | Magnitude |
|---|---|---|---|
| SDSS-$u$ | 3546 | 558 | $18.361 \pm 0.039$ |
| Johnson-$B$ | 4378 | 1158 | $16.8 \pm 0.1$ |
| SDSS-$g$ | 4670 | 1158 | $16.283 \pm 0.004$ |
| Johnson-$V$ | 5466 | 890 | $15.9 \pm 0.1$ |
| SDSS-$r$ | 6156 | 1111 | $15.464 \pm 0.003$ |
| Johnson-$R$ | 6696 | 2070 | $15.3 \pm 0.1$ |
| SDSS-$i$ | 7471 | 1045 | $15.146 \pm 0.003$ |
| WFCAM-$Z$ | 8802 | 927 | $14.501 \pm 0.003$ |
| SDSS-$z$ | 8918 | 1124 | $14.959 \pm 0.005$ |
| WFCAM-$Y$ | 10339 | 999 | $14.352 \pm 0.004$ |
| 2MASS-$J$ | 12350 | 1624 | $13.928 \pm 0.025$ |
| WFCAM-$J$ | 12490 | 1513 | $13.963 \pm 0.003$ |
| WFCAM-$H$ | 16338 | 2810 | $13.470 \pm 0.002$ |
| 2MASS-$H$ | 16620 | 2509 | $13.464 \pm 0.026$ |
| 2MASS-$K_s$ | 21590 | 2619 | $13.414 \pm 0.039$ |
| WFCAM-$K$ | 22185 | 3251 | $13.360 \pm 0.003$ |
| WISE-$W1$ | 34002 | 6626 | $13.292 \pm 0.027$ |
| WISE-$W2$ | 46520 | 10422 | $13.368 \pm 0.038$ |
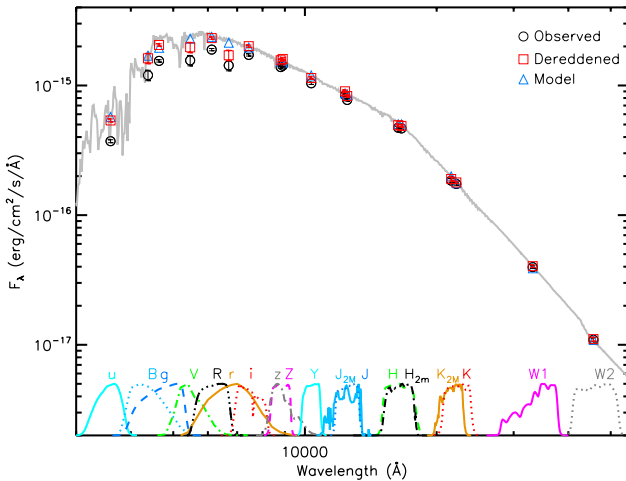


**Figure 2.** The SED of WTS-2. The best-fitting Kurucz model spectrum from a $\chi^2$ analysis (see Section 4.1) is overlaid in grey ($T_{eff} = 5000\,K$), while the synthetic photometry for the corresponding observed bandpasses are shown by the blue open triangles. The observed data are shown by the black open circles and the dereddened photometry is shown by the red open squares. Note that the errors on the photometry include the photon error listed in Table 2, plus a 2 per cent uncertainty added in quadrature to the WFCAM and SDSS bandpasses to allow for calibration between the different surveys. However, the magnitudes have not been adjusted for contamination by a faint red source of third light within 0.6 arcsec of the host star (see Section 3.5) The symbols are generally bigger than the errors. The filter transmission profiles for our observed bandpasses (see Table 2) are shown by the lines at the bottom of the plot.
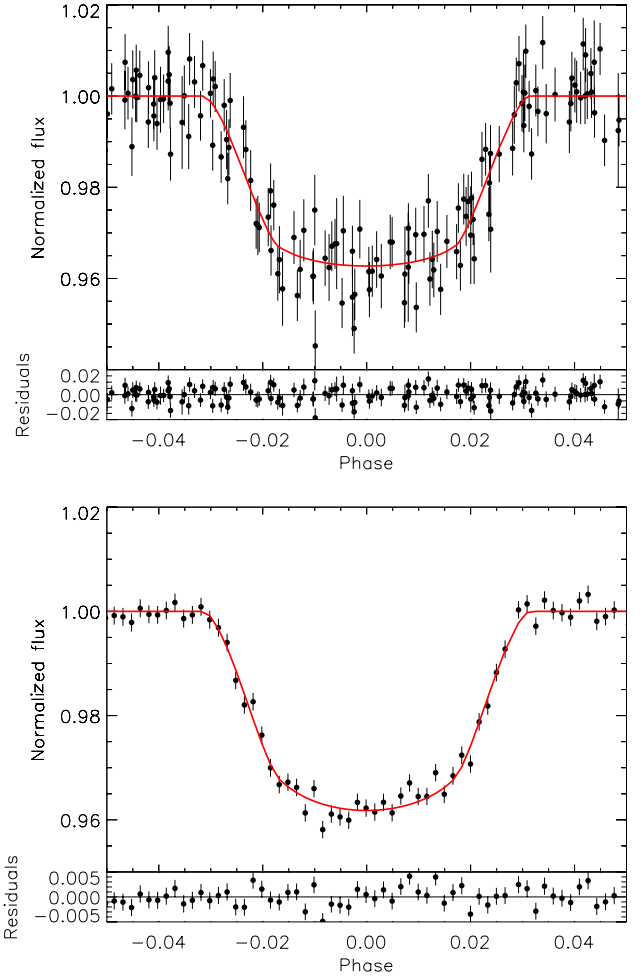


**Figure 3.** Top: phase-folded WTS $J$-band light curve for WTS-2 b corrected for dilution by a faint red source and zoomed around the transit. The adopted best model from a simultaneous fit to the $J$- and $i$-band dilution-corrected light curves is shown by the solid red line (see Section 5.1). The errors have been scaled such that the out-of-transit data has $\chi_\nu^2 = 1$ when compared to a flat line. The lower panel shows the residuals to the model. Bottom: same as above but for the dilution-corrected INT $i$-band light curve. All the available data are shown. Note the change in $y$-axis scale for the residuals.

autoguider to place the star back on to the exact same pixel after every exposure).

The Cambridge Astronomical Survey Unit (CASU) INT/WFC data reduction pipeline (Irwin & Lewis 2001; Irwin et al. 2007) was used to reduce the $i$-band images. The pipeline follows a standard CCD reduction of de-biasing, correcting for non-linearity, flat-fielding and defringing. A master source catalogue was extracted from a stacked image of the 20 best frames and variable aperture photometry was performed for all sources in all images to generate light curves. The out-of-transit rms in the WTS-2 $i$-band light curve is 1.5 mmag. The light curve is used simultaneously with the $J$-band light curve to find the best-fitting model transit to WTS-2 b in Section 5.1. The WTS-2 b $i'$-band light curve is shown in Fig. 3 and the data are given in Table 3.

### 3.3 CAHA/TWIN intermediate-resolution spectroscopy

We carried out intermediate-resolution reconnaissance spectroscopy of WTS-2 to obtain an estimate of the host star effective

**Table 3.** The observed INT *i*-band light curve for WTS-2 b without correction for dilution. The errors were derived in the same manner as for the *J* band but have been scaled so that the out-of-transit baseline has a reduced $\chi^2 = 1$ when compared to a flat line to avoid underestimating the errors (see Fig. 3). (This table is published in full in the online paper and is shown partially here for guidance regarding its form and content.)

| HJD | Normalized flux | Error |
|---|---|---|
| 245 5396.564 493 61 | 1.0047 | 0.0015 |
| 245 5396.567 549 40 | 0.9988 | 0.0015 |
| – | – | – |

**Table 4.** Reconnaissance RVs from CAHA 3.5 m/TWIN.

| HJD | RV (km s$^{-1}$) | $\sigma_{RV}$ (km s$^{-1}$) |
|---|---|---|
| 245 5721.417 173 | −19.794 | 1.540 |
| 245 5721.501 447 | −19.122 | 2.015 |
| 245 5721.586 693 | −19.091 | 1.820 |
| 245 5762.651 947 | −19.050 | 1.888 |
| 245 5762.659 494 | −18.415 | 1.670 |
| 245 5763.590 589 | −21.118 | 1.560 |
| 245 5763.658 298 | −20.079 | 1.614 |
| 245 5763.665 845 | −18.796 | 1.656 |
| 245 5783.377 699 | −22.410 | 1.599 |
| 245 5783.567 465 | −19.215 | 1.374 |
| 245 5783.645 763 | −18.072 | 1.888 |
| 245 5783.656 805 | −19.118 | 1.851 |
| 245 5784.508 995 | −19.121 | 1.132 |
| 245 5784.661 690 | −20.206 | 1.710 |
| 245 5784.672 731 | −20.004 | 1.313 |
| 245 5785.444 262 | −19.560 | 1.265 |
| 245 5785.508 347 | −21.585 | 1.863 |
| 245 5785.668 461 | −19.728 | 1.971 |

temperature and its surface gravity (see Section 4), and to measure preliminary RV variations to test for the presence of a blended or grazing eclipsing binary system (see Section 6 and Table 4). Spectroscopic observations of WTS-2 and several RV standards were taken over six nights during 2011 June–August as part of a wider follow-up campaign of the WTS planet candidates and M-dwarf eclipsing binaries (Cruz et al., in preparation). We used the Cassegrain Twin Spectrograph (TWIN) mounted on the 3.5 m telescope at the Calar Alto Observatory (CAHA) in southern Spain, with its T10 grism and a 1.2 arcsec slit, resulting in a dispersion of ∼0.39 Å pix$^{-1}$ ($R \sim$ 8000) and a wavelength coverage of ∼ 6200−6950 Å. A total of 18 epochs were observed for WTS-2 with integration times between 600 and 900 s.

The spectra were reduced in the standard way using IRAF packages. To measure the RV variations of WTS-2 and the RV standards, the IRAF package FXCOR was used to perform Fourier cross-correlation of the observed spectra with synthetic templates generated from Munari et al. (2005). The effective temperature and surface gravity of the cross-correlation template was chosen to match the results of the SED fit in Section 4 but with a solar metallicity. We also use the TWIN spectra in Section 4 to confirm the stellar characteristics found via the SED fit. For this, we used a spectrum created by aligning and stacking eight of the TWIN spectra obtained
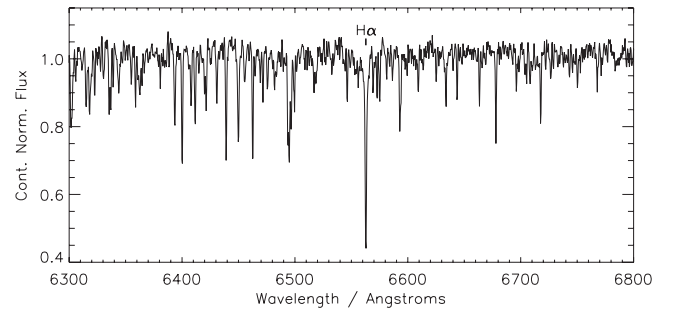


**Figure 4.** A stacked spectrum of WTS-2 using eight of the TWIN observations from 2011 August. The individual spectra have been aligned to the same RV and continuum normalized. The rest wavelength of Hα is labelled.

in 2011 August into a single spectrum with SNR∼25. The stacked spectrum is shown in Fig. 4.

### 3.4 HET high-resolution spectroscopy

High-resolution spectroscopic observations of WTS-2 were obtained during 2011 August–November at the McDonald Observatory in Austin, Texas, using the High Resolution Spectrograph (HRS; Tull 1998) at the Hobby-Eberly Telescope (HET). These spectra were used to measure the RV variations of the star and hence calculate the Keplerian parameters of the WTS-2 spectroscopic orbit (see Section 5.2), and to measure the bisector variations to help assess false-positive scenarios (see Section 6). The relative faintness of WTS-2 necessitated a large aperture telescope in order to achieve high-precision RV measurements. HET has an effective aperture of 9.2 m (Ramsey et al. 1998) and sits at a fixed elevation angle of 55°, rotating in azimuth to access 81 per cent of the sky visible from the observatory. HRS is a single-object fibre-coupled spectrograph with two additional sky fibres that uses a mosaic of two R-4 echelle gratings with cross-dispersing gratings to separate the spectral orders. We used an effective slit width of 2 arcsec with the 600g5271 grating to give a resolution of $R = 60\,000$ and a wavelength coverage of ∼4400−6280 Å, separated into 40 echelle orders across the two CCD detectors (18 on the red CCD and 22 on the blue CCD). Each science image was a 1 h integration, split into 2 × 30 min exposures. Due to the faintness of the star, we did not use the iodine gas cell but instead observed several exposures of the ThAr arc lamp before and after each science frame for wavelength calibration and to monitor any systematic shifts. A high SNR exposure of a white dwarf was also obtained as a telluric standard.

The IRAF.ECHELLE[4] package was used to reduce the HET spectra. After subtracting the bias and flat-fielding the images, the science and sky spectra for each 30 min exposure were extracted order by order, and the corresponding sky spectrum was then subtracted. Wavelength calibration was achieved using the extracted ThAr arc lamp spectra. The dispersion functions calculated for the ThAr spectra (rms ∼ 0.003 Å) taken before and after the science frames were checked for consistency and then linearly interpolated to create a final dispersion function to apply to the stellar spectra. No significant drift or abnormalities were observed in the wavelength solution during each observing run. Before combining the two 30-min exposures at each epoch, the individual spectra were continuum normalized, filtered for residual cosmic rays, and corrected for telluric features

---

[4] http://iraf.net/irafdocs/ech.pdf

**Table 5.** RV data for WTS-2 derived from the HET/HRS spectra and their associated bisector span (BS) variations (see Section 6). The error on each RV data point $\sigma_{RV}$ in this table is the standard deviation on the mean of measured RVs across all echelle orders for that epoch. The phases are calculated using the best-fitting period from the simultaneous light-curve analysis in Section 5.1.

| HJD | Phase | RV (km s$^{-1}$) | $\sigma_{RV}$ (km s$^{-1}$) | BS (km s$^{-1}$) | $\sigma_{BS}$ (km s$^{-1}$) |
|---|---|---|---|---|---|
| 245 5790.832 53 | 0.9599 | $-19.922$ | 0.043 | 1.73 | 0.90 |
| 245 5822.737 90 | 0.2790 | $-20.332$ | 0.061 | 0.83 | 0.93 |
| 245 5845.680 06 | 0.7997 | $-19.761$ | 0.046 | 0.72 | 0.95 |
| 245 5856.650 80 | 0.5693 | $-20.021$ | 0.047 | $-0.44$ | 0.81 |
| 245 5867.617 87 | 0.3349 | $-20.295$ | 0.051 | 0.04 | 0.90 |
| 245 5869.614 45 | 0.2952 | $-20.282$ | 0.048 | $-0.48$ | 0.75 |
| 245 5876.596 97 | 0.1490 | $-20.115$ | 0.040 | 0.08 | 0.86 |

at the redder wavelengths (using the extracted white dwarf spectrum) using a custom set of MATLAB programs. After combining the exposures at each epoch we obtained a total of seven spectra with average SNRs of ∼15.

We note here that due to the faintness of WTS-2, the cores of the deepest lines in the HRS spectra are distorted during the calibration process, particularly after sky subtraction. This means only the weaker lines in these high-resolution spectra are suitable for any detailed spectroscopic analysis of the host star, such as abundance calculations or measuring the projected rotational velocity (see Section 4).

To measure the RVs, each echelle order in the spectrum was cross-correlated with a synthetic template using IRAF.FXCOR. The template was taken from the MAFAGS-OS grid of model atmospheres (Grupp 2004) with $T_{eff} = 4800$ K, $\log(g) = 4.5$ and solar metallicity. The template parameters are within the errors of the final host star properties obtained by the detailed analysis in Section 4, and the variation of the RVs for different templates within these errors is negligible compared to the errors on the measured RVs. The RVs reported in Table 5 and shown in Fig. 5 are the mean RV from all the echelle orders at a given epoch with the uncertainties equal to the standard deviation on the mean of the RVs.

### 3.5 High-resolution *i*/*z*-band AstraLux/CAHA lucky imaging

Although the WFCAM *J*-band survey images are of relatively high spatial resolution (0.4 arcsec pix$^{-1}$) compared to most ground-based transit surveys, in order to adequately address false-positive scenarios and search for unresolved stellar companions, we obtained high-resolution images of WTS-2 with the lucky imaging camera AstraLux (Hormuth et al. 2008) mounted on the CAHA 2.2 m telescope. The observations were carried out on the night of 2013 June 14, with a mean seeing of 0.6 arcsec. We obtained 30 000 frames in the *i* and *z* bands with single frame exposure times of 0.08 and 0.06 s, respectively. The basic reduction, frame selection and image combination were carried out with the AstraLux pipeline[5] (Hormuth 2007). During the reduction process, the images are resampled to half their pixel size. The calculated plate solution is then $23.61 \pm 0.20$ mas pixel$^{-1}$ (Lillo-Box et al., submitted). The plate scale was measured with the CCMAP package of IRAF by matching the *XY* positions of 66 stars identified in an AstraLux image with their counterparts in the Yanny et al. (1994) catalogue
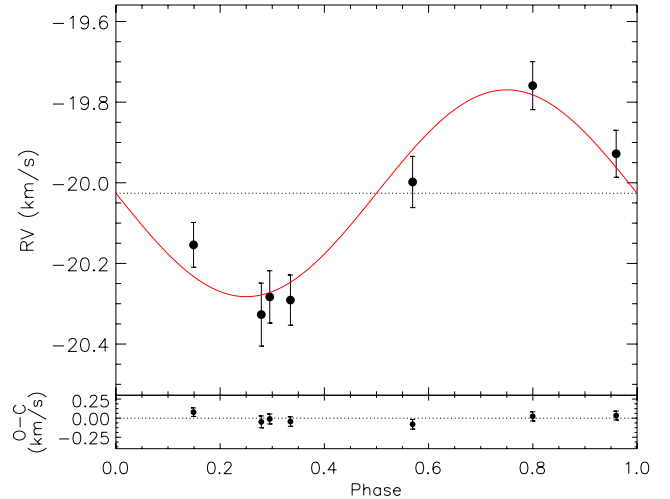
**Figure 5.** Top: the RV curve of WTS-2 as a function of the orbital phase, measured using high-resolution spectra from HET. The red solid curve shows the best-fitting model to the data ($K_\star = 256 \pm 32$ m s$^{-1}$, see Section 5.2), while the dotted horizontal line marks the measured systemic velocity of the system. The best-fitting model parameters are given in Table 6. A circular orbit was assumed in the model. The RV error bars in this plot have been scaled such that the fit gives $\chi^2_\nu = 1$. Bottom: residuals after subtracting the best-fitting model.
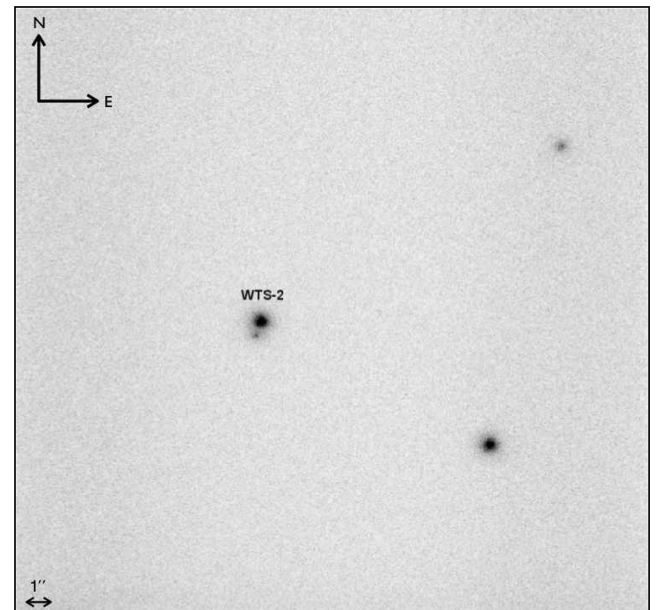


**Figure 6.** AstraLux *z*-band image of WTS-2 and two other bright stars in the field. The field of view is $24 \times 24$ arcsec. A faint source is clearly visible $0.567 \pm 0.005$ arcsec South of WTS-2.

of the *Hubble Space Telescope* (see Lillo-Box, Barrado & Bouy 2012 for a more detailed explanation of this method which was used to study ∼100 *Kepler* planet host candidates). For our analysis, we used the best 1 per cent of exposures in the *i* and *z* bands, which have point spread functions (PSFs) with FWHMs of 0.24 and 0.18 arcsec, respectively. Fig. 6 shows the *z*-band stack in which a faint source is visible $0.567 \pm 0.005$ arcsec south of WTS-2. We performed an iterative PSF fitting of WTS-2 and this nearby source to estimate the flux of each of them. The PSF was constructed using the two brighter sources in the field of view. We find

that the nearby faint source is contributing 10.4 ± 1.0 and 13.1 ± 1.0 per cent of the total light in the *i* and *z* bands, respectively. We can exclude any other companions beyond a projected separation of 0.4 arcsec from WTS-2 down to a magnitude difference of $\Delta m = 3$ mag at the $3\sigma$ level.

Motivated by this result, we extended our analysis to *ZYJHK*-band images taken with WFCAM (see Section 3.1). Although these data have a significantly larger pixel scale (0.4 arcsec pixel$^{-1}$) and considerably larger PSFs (FWHM ∼ 1.2–1.7 arcsec), we were able to perform a simultaneous fit of two PSFs and estimated in this way the blending light coming from the faint source that is located of WTS-2. For the PSF fitting we made use of the position information we obtained from the high-resolution AstraLux images by restricting the separation and position angle to the one measured on the *i*- and *z*-band images. For the five WFCAM bands we find that the faint source is contributing 9.5 ± 3.0, 10.7 ± 4.0, 19.0 ± 4.0, 19.8 ± 4.0, and 22.5 ± 3.0 per cent in the *Z*, *Y*, *J*, *H* and *K* bands, respectively.

The resulting magnitudes for the contaminant are thus as follows: SDSS-*i* = 17.66 mag, WFCAM-*Z* = 17.12 mag, SDSS-*z* = 17.14 mag, WFCAM-*Y* = 16.97 mag, WFCAM-*J* = 15.77 mag, WFCAM-*H* = 15.23 mag, and WFCAM-*K* = 14.98 mag. The *H* − *K* and *J* − *H* colours of the contaminant correspond to a spectral type of ∼M1V and $T_{\mathrm{eff}}$ ∼ 3600 K when compared with the Baraffe et al. (1998) models. This situation is similar to the hot Jupiter WASP-12b which was also recently shown to be diluted by a faint M dwarf at 1 arcsec separation (Crossfield et al. 2012). If the M dwarf in our aperture is gravitationally bound to the K dwarf, the projected separation would correspond to an orbital separation of ∼600 au, and an orbital period of ∼12 500 yr, assuming a face-on, circular orbit. To assess the likelihood of physical association between the two sources, we estimated the probability that the faint source is a chance alignment star using the Besançon stellar population synthesis models (Robin et al. 2003). We extracted the predicted number of stars in a 1.6 sq. degree region centred on the coordinates of WTS-2 in the magnitude range of the faint source (*I* = 16.95–17.1 mag, where the SDSS *i* magnitude was converted to *I* using the relations on the SDSS website$^6$). In this range, we find 2 × 10$^{-4}$ stars per sq. arcsec. Multiplying this by our aperture area ($\pi$(2 arcsec)$^2$), we find a priori probability of <0.26 per cent of finding a suitably faint red star in our aperture. This value is a factor of 10 lower if one only considers stars within the projected separation of the WTS-2 and the faint source. We therefore conclude that the faint source is likely to be a wide-orbit companion to WTS-2, however the small proper motion means confirmation of physical association could take many years.

# 4 CHARACTERIZATION OF THE HOST STAR

The properties of the planet WTS-2 b depend directly on the characterization of its host star. Due to the faintness of the host star, the usual method of deriving the stellar parameters from very high resolution spectra (see e.g. Torres et al. 2012) is not appropriate because the SNR in our high-resolution HET spectra is too low, and furthermore the previously mentioned issue of distorted features in the cores of the deepest lines could bias the results. Instead, we use two data sets of lower resolution and complementary analyses to arrive at consistent estimates of the stellar properties, albeit with

---

$^6$ http://www.sdss.org/dr5/algorithms/sdssUBVRITransform.html#Lupton2005

comparatively larger uncertainties. Table 6 gives the final adopted parameters and their errors based on the results of this section.

We note here that we have not corrected the following analysis for contamination by the faint red source within the aperture or slit of the observations. The majority of this analysis is based on data at optical wavelengths where the contribution from the faint red source is low (<10 per cent), hence our derived host star properties are unlikely to deviate outside the presented uncertainties when accounting for the faint red source.

## 4.1 Effective temperature, surface gravity, metallicity, lithium abundance, and rotation

### 4.1.1 Photometric analysis

To begin, we refined the initial SED fit to the WFCAM photometry using VOSA to add more bandpasses and to explore a wider range of $T_{\mathrm{eff}}$, surface gravities, metallicities, and to fit for reddening. VOSA calculates synthetic photometry by convolving theoretical atmospheric models with the filter transmission curves of the observed bandpasses, then performs a $\chi^2$ minimization to find the best-fitting model to the data (Bayo et al. 2008, 2013). We used a grid of Kurucz ATLAS9 model spectra (Castelli, Gratton & Kurucz 1997) in the range $3500 \leq T_{\mathrm{eff}} \leq 6000$ K in steps of 250 K, with $\log(g) = 4.0 - 5.0$ in steps of 0.5 dex (to be consistent with the light-curve stellar density estimate), [Fe/H] = [−0.5, 0.0, +0.2, +0.5], and $0 \leq A_V \leq 0.5$ in steps of 0.025. The upper boundary on the extinction range was chosen to approximately match the total integrated line-of-sight extinction for the $2°$ region around the centre of the 19 h field ($A_V = 0.439$ mag, $E(B - V) = 0.132$ mag), calculated using the infrared dust maps of Schlegel, Finkbeiner & Davis (1998). Fig. 2 shows the best-fitting SED for WTS-2, which has a reduced $\chi_\nu^2 = 3.9$. Note that a 2 per cent error was added in quadrature to the SDSS and WFCAM photometric errors given in Table 2, to allow for calibration between the surveys, but that the magnitudes have not been corrected for the presence of the faint red source within 0.6 arcsec of the brighter star (see Section 3.5). In addition to the $\chi^2$ model fit, VOSA performs a Bayesian analysis of the model fit, resulting in a posterior probability density function covering the range of fitted values for each parameter. A Gaussian-fit to the $T_{\mathrm{eff}}$ and $A_V$ distributions gives approximate errors as follows: $T_{\mathrm{eff}} = 5000 \pm 140$ K and $A_V = 0.27 \pm 0.07$. For $\log(g)$ the distribution is essentially flat due to the intrinsic insensitivity of the available broad-band photometry to gravity sensitive features, so we adopt $\log(g) = 4.5 \pm 0.5$. For [Fe/H], higher metallicity is preferred, with the most probable solutions being [Fe/H] = +0.2 and +0.5 (37 and 42 per cent, respectively). The $T_{\mathrm{eff}}$ from the refined SED fit is higher than our original estimate, which is not surprising given that the initial estimate was made using models known to underestimate $T_{\mathrm{eff}}$ for stars earlier than M type.

### 4.1.2 Spectroscopic analysis

We checked the results of the SED fitting in two ways; first by fitting synthetic spectra to the stacked TWIN spectrum, and secondly through a standard spectroscopic abundance analysis of the same spectrum. From the latter, we also derived estimates of the rotational and microturbulence velocities, and an upper limit on the lithium abundance. First, we compared the stacked TWIN spectrum of WTS-2 to synthetic spectra in the Coelho et al. (2005) library. The spectral library was generated by the PFANT code (Barbuy et al. 2003), which computes the synthetic spectra using the updated

**Table 6.** Characterization of the WTS-2 system. The 'Dilution-corrected' column is based on an analysis in which the light curves were corrected for contamination by a faint red source contributing $10.4 \pm 1$ and $19.0 \pm 4$ per cent of the flux in the aperture in the *i* and *J* bands, respectively (see Section 3.5). The 'Diluted' column gives the results without correction for the faint red source. The errors on the light-curve parameters are the 68.3 per cent confidence interval while the parameter value is the mean of the 68.3 per cent confidence level boundaries, such that the errors are symmetric. Despite its KIC name, WTS-2 b is unfortunately not in the *Kepler* field of view.

| Stellar properties: | Diluted | *Dilution corrected* |
|---|---|---|
| Names | WTS-2 | – |
| | 2MASS 19345587+3648557 | – |
| | SDSS J193455.87+364855.6 | – |
| | WISE J193455.86+364855.6 | – |
| | KIC 1173581 | – |
| RA | $19^{\rm h}34^{\rm m}55\overset{\rm s}{.}87$ ($293\overset{\circ}{.}732792$) | – |
| Dec. | $+36°48'55''79$ ($36\overset{\circ}{.}815497$) | – |
| $T_{\rm eff}$ | $5000 \pm 250$ K | – |
| Spectral type | K2($\pm$2)V | – |
| $\log(g)^a$ | $4.5 \pm 0.5$ | – |
| $\log(g)^b$ | $4.589 \pm 0.023$ | $4.600 \pm 0.023$ |
| [Fe/H] | $+0.2^{+0.3}_{-0.2}$ | – |
| $v\sin(i)$ | $2.2 \pm 1.0$ km s$^{-1}$ | – |
| $\xi$ | $0.75 \pm 0.5$ km s$^{-1}$ | – |
| $\log N({\rm Li})_{\rm LTE}$ | $<1.8$ dex | – |
| $M_\star^b$ | $0.820 \pm 0.082$ M$_\odot$ | $0.820 \pm 0.082$ M$_\odot$ |
| $R_\star^b$ | $0.761 \pm 0.033$ R$_\odot$ | $0.752 \pm 0.032$ R$_\odot$ |
| $\rho_\star^c$ | $1.86 \pm 0.15\rho_\odot$ | $1.93 \pm 0.16\rho_\odot$ |
| $R_{\rm cz}$ | $\sim$0.54 R$_\odot$ | $\sim$0.54 R$_\odot$ |
| $M_{\rm cz}$ | $\sim$0.05 M$_\odot$ | $\sim$0.05 M$_\odot$ |
| Age | $>600$ Myr | – |
| $A_V$ | $0.27 \pm 0.07$ mag | – |
| Distance | $\sim$1 kpc | – |
| $\mu_\alpha\cos\delta$ | $2.3 \pm 2.3$ mas yr$^{-1}$ | – |
| $\mu_{\rm delta}$ | $-1.9 \pm 2.3$ mas yr$^{-1}$ | – |
| $U$ | $-13.3 \pm 5.6$ km s$^{-1}$ | – |
| $V$ | $-0.3 \pm 7.7$ km s$^{-1}$ | – |
| $W$ | $-15.1 \pm 5.3$ km s$^{-1}$ | – |

| System properties: | Diluted | *Dilution corrected* |
|---|---|---|
| $P$ | $1.0187074 \pm 7.1 \times 10^{-7}$ d | $1.0187068 \pm 6.5 \times 10^{-7}$ d |
| $T_0 - 2454317$ | $0.81264 \pm 6.4 \times 10^{-4}$ HJD | $0.81333 \pm 6.5 \times 10^{-4}$ HJS |
| $R{\rm p}/R_\star$ | $0.1755 \pm 0.0018$ | $0.1863 \pm 0.0021$ |
| $b$ | $0.597 \pm 0.032$ | $0.584 \pm 0.033$ |
| $i$ | $83.43 \pm 0.53°$ | $83.55 \pm 0.53°$ |
| $a$ | $0.01855 \pm 0.00062$ au | $0.01855 \pm 0.00062$ au |
| | $1.51 \pm 0.11a_{\rm Roche}$ | $1.44 \pm 0.12a_{\rm Roche}$ |
| $\bar{\chi}^2_{\rm LC}$ | 457.8 | 387.2 |
| $K$ | $256 \pm 32$ m s$^{-1}$ | – |
| $V_{\rm sys}$ | $-20.026 \pm 0.019$ km s$^{-1}$ | – |
| $e$ | 0 (fixed) | – |

| Planet properties: | Diluted | *Dilution corrected* |
|---|---|---|
| $M_{\rm P}$ | $1.12 \pm 0.16M_{\rm J}$ | $1.12 \pm 0.16M_{\rm J}$ |
| $R_{\rm p}$ | $1.300 \pm 0.058R_{\rm J}$ | $1.363 \pm 0.061R_{\rm J}$ |
| $\rho_{\rm P}$ | $0.63 \pm 0.12$ g cm$^{-3}$ ($0.477 \pm 0.093\rho_{\rm J}$) | $0.54 \pm 0.11$ g cm$^{-3}$ ($0.413 \pm 0.080\rho_{\rm J}$) |
| $g_b$ | $16.4 \pm 2.7$ ms$^{-2}$ | $14.9 \pm 2.5$ ms$^{-2}$ |
| $F_{\rm inc}$ | $1.29 \times 10^9 \pm 0.29 \times 10^{-9}$ erg s$^{-1}$ cm$^{-2}$ | $1.26 \times 10^9 \pm 0.29 \times 10^{-9}$ erg s$^{-1}$ cm$^{-2}$ |
| $T_{\rm eq}^d$ | $2000 \pm 100$ K | $2000 \pm 100$ K |
| $\Theta$ | $0.0389 \pm 0.0070$ | $0.0371 \pm 0.0068$ |

$^a$From spectroscopic analysis. $^b$From light-curve mean stellar density and stellar evolution isochrones. $^c$From light-curve analysis. The proper motions $\mu_\alpha\cos\delta$ and $\mu_{\rm delta}$ are from the SDSS DR7 data base. The space velocities $U, V, W$ are with respect to the Sun (heliocentric) but for a left-handed coordinate system, i.e. U is positive away from the Galactic Centre. $\bar{\chi}^2_{\rm LC}$ is the mean of the $\chi^2$ values in the MCMC runs. $^d$Equilibrium temperature assuming $A_B = 0$ and $f = 2/3$. Note that we used the equatorial radius of Jupiter ($R_{\rm J} = 7.1492 \times 10^7$ m). $a_{\rm Roche}$ is the Roche limit separation, i.e. the critical distance inside which the planet would lose mass via Roche lobe overflow. $g_b$ is the planet surface gravity according to equation 7 in Southworth ([2008]). $\Theta$ is the Safronov number ($\Theta = \frac{1}{2}(V_{\rm esc}/V_{\rm orb})^2 = (a/R_P)(M_P/M_\star)$) (Hansen & Barman [2007]).

ATLAS9 model atmospheres of Castelli & Kurucz (2004) (with a mixing length equal to twice the scaleheight) and a list of atomic and molecular lines, under the assumption of local thermodynamic equilibrium (LTE). Before we performed a $\chi^2$ minimization to find the best-fitting model, the synthetic spectra were degraded to the resolution of the TWIN spectra, then normalized to their continuum along with the observed stacked spectrum. Our model grid covered $4250 \leq T_{\mathrm{eff}} \leq 5500$ K in steps of 250 K, $4.0 \leq \log(g) \leq 5.0$ in steps of 0.5, and [Fe/H] = [−1.0, −0.5, 0.0, +0.2, +0.5]. We noted that the synthetic spectra systematically underpredicted the depth of some absorption features in the solar spectrum (most likely due to neglect of non-LTE effects and/or errors in the continuum normalization) such that our $\chi^2$ minimization would preferentially select metal-rich spectra (see Cappetta et al. 2012 for a more detailed explanation). We therefore only performed the $\chi^2$ analysis on those lines that were well reproduced for the solar spectrum. The best-fitting model was consistent with the VOSA result, giving $T_{\mathrm{eff}} = 5000 \pm 250$ K, $\log(g) = 4.5 \pm 0.5$, and [Fe/H] $= +0.2^{+0.3}_{-0.2}$, where the errors correspond simply to the step-size in the models. This corresponds to a spectral type of K2V±2, according to table B1 of Gray (2008).

For the standard spectroscopic abundance analysis, we measured the excitation potential of neutral Fe I and ionized Fe II lines in the TWIN stacked spectrum and compared them to synthetic spectra. All synthetic spectra were calculated using 1D LTE model atmospheres computed with SAM12 and WITA6 routines (Pavlenko 2003) and constants taken from the VALD2 (Kupka et al. 1999). For a complete description of our procedure, see Pavlenko et al. (2012). For a range of synthetic models with microturbulence velocity $\xi = 0.0$–$2.5$ km s$^{-1}$, in steps of 0.25 km s$^{-1}$, and $T_{\mathrm{eff}} = 4900$–$5100$ K in steps of 100 K, we found that the ionization equilibrium condition was met at $\xi = 0.75 \pm 0.50$ for $\log(g) = 4.45 \pm 0.25$. The corresponding iron abundance was [Fe/H] $= +0.095 \pm 0.021$, again consistent with the SED-fitting results.

To measure the rotational velocity of the star, the $v \sin(i)$ value was calculated independently for each of the 20 Fe II lines in the TWIN stacked spectrum, by convolving the model line profile with a set of rotation profiles (Gray 2008), ranging from 0 to 6 km s$^{-1}$ in steps of 0.2 km s$^{-1}$. The average and standard deviation of all the lines was $v \sin(i) = 2.2 \pm 1.0$ km s$^{-1}$. Finally, we placed an upper limit on the lithium abundance of $\log N(\mathrm{Li}) < 1.8$ ($= 12 + \log N(\mathrm{Li/H})$), with an equivalent width upper limit of EW(Li) $\sim$ 0.089 Å. Only upper limits are possible due to noise contamination and relatively low resolution of the TWIN spectrum (see Fig. 7).

## 4.2 Mass and age constraints

The mass of WTS-2 was derived using a modified Hertzsprung–Russell diagram, as shown in Fig. 8, comparing the spectroscopically measured $T_{\mathrm{eff}}$ to the stellar density measured from the light curves. Model isochrones were generated using the PAdova and TRieste Stellar Evolution Code (PARSEC) v1.0 code, which includes the pre-main-sequence phase (Bressan et al. 2012), for $Z = 0.019$ (i.e. solar). The observational errors on $T_{\mathrm{eff}}$ allow solutions in the pre-main-sequence phase; however, we rule out young ages using other indicators. For example, comparing the upper limit on the lithium abundance of WTS-2 to that observed in open clusters of a known age (Sestito & Randich 2005), constrains the age to >250 Myr. This already places the system beyond the pre-main-sequence phase of the isochrones. For K dwarfs, one can also obtain age constraints via gyrochronology (Barnes 2007; Mamajek & Hillenbrand 2008), which depends on the stellar rotation period,
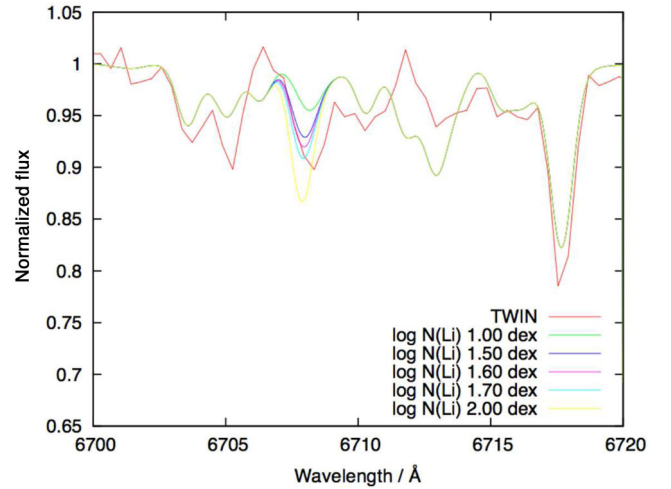


**Figure 7.** A section of the stacked TWIN spectrum covering the lithium feature at 6707.55–6709.21 Å with models overlaid for different Li abundances. The apparent redshift of the observed Li feature is most likely due to noise contamination, so we place an upper limit at $\log N(\mathrm{Li})_{\mathrm{LTE}} = 1.8$ dex.
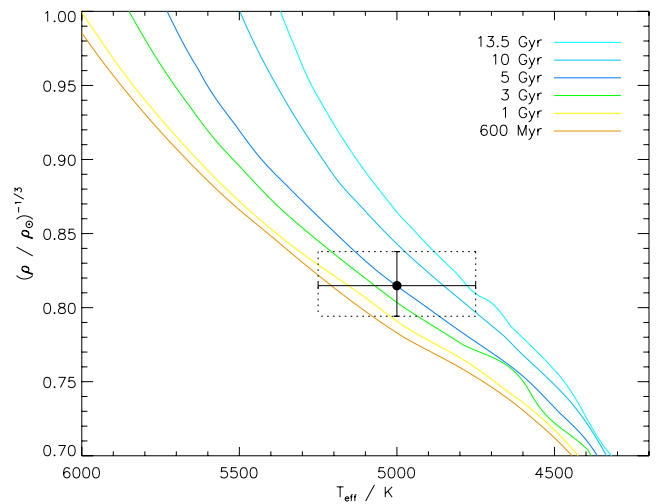


**Figure 8.** Modified Hertzsprung–Russell diagram comparing the effective temperature and light-curve stellar density for WTS-2, with the PARSEC v1.0 stellar evolution isochrones (Bressan et al. 2012) for $Z = 0.019$. The data point and its error box marks the allowed values for WTS-2. Assuming the star is not on the pre-main sequence, the isochrones give an age constraint of >600 Myr.

usually measured from star spot modulation in the light curve. However, all significant peaks in the WTS-2 periodogram are consistent with aliases of the observing window function or of long-term systematic trends present in all the WTS light curves. This is not surprising, given that we are using infrared light curves, which have less contrast between the spot and stellar temperatures, resulting in lower amplitude rotational modulation signals (Goulding et al. 2012). However, the maximum possible rotation period is set by the upper limit on $v \sin(i)$ (3.2 km s$^{-1}$ for WTS-2). Using equation 7 of Maldonado et al. (2010), we find that the upper limit on $v \sin(i)$ is consistent with a gyrochronology lower age limit of $\gtrsim 600$ Myr. Our spectra do not cover sufficient activity sensitive spectral features so we cannot use the age–activity relationship, although the lack of emission in the H$\alpha$ line rules out a very young star. However, the
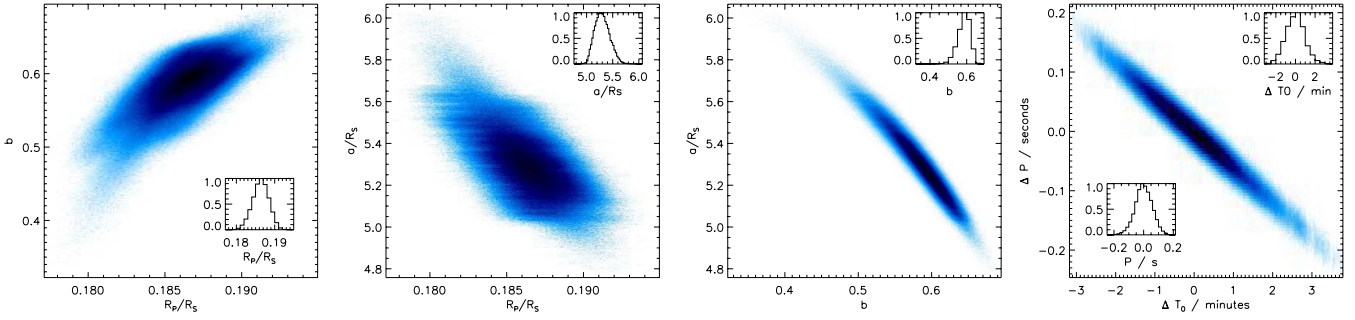
**Figure 9.** Distributions of correlated parameters in the MCMC analysis of the dilution-corrected light curves. The insets show individual parameter (normalized) histograms to highlight the skew in the distributions.

age constraint is consistent with the young and young–old Galactic disc (Leggett 1992), determined from the space velocities given in Table 6, which were derived using proper motions from SDSS DR7 (Munn et al. 2004, 2008) and the systemic velocity derived in Section 5.2. The model isochrones between 0.6 and 13.5 Gyr allow a mass range of $M_\star = 0.820 \pm 0.082\,M_\odot$, which we adopt as the mass of WTS-2. As a K dwarf, WTS-2 has a deeper outer convective envelope than the Sun. According to the models of van Saders & Pinsonneault (2012), the physical depth of the convective envelope is at $R_{cz} \sim 0.54\,R_\odot$ (~30 per cent of the stellar radius), and it has a mass of $M_{cz} \sim 0.05\,M_\odot$ according to the Pinsonneault, DePoy & Coffee (2001) models (compared to $M_{cz} \sim 0.001\,M_\odot$ for a late F star such as WASP-18).

## 5 SYSTEM PARAMETERS

The orbital elements and physical properties of WTS-2 b are derived from a simultaneous fitting of the *J*- and *i*-band light curves, then combining the results with a separate analysis of the RVs measured with HET. Given that we have an estimate of the blended light contribution in both the *i*- and *J*-band filters, we present an analysis of both the diluted and dilution-corrected light curves for completeness. We adopt the dilution-corrected solution for the remainder of this paper; however, many of the derived parameters are consistent within the 1σ error bars from both analyses due to the relatively large errors on the fractions of blended light. We also address the limits we can place on the *J*-band secondary eclipse of WTS-2 b.

### 5.1 Light-curve analysis

In both the diluted and dilution-corrected cases, the *J*- and *i*-band light curves were modelled jointly using the analytic formulae presented by Mandel & Agol (2002). A Markov chain Monte Carlo (MCMC) analysis was used to derive the uncertainties on the fitted parameters and their correlations. We fixed the limb-darkening coefficients in the fit by adopting values from the tables of Claret & Bloemen (2011). We used the ATLAS atmospheric models and the flux conversion method to obtain the quadratic law limb-darkening coefficients in the *i* and *J* bands ($\gamma_{1i}, \gamma_{2i}, \gamma_{1J}, \gamma_{2J}$) corresponding to $T_{eff} = 5000\,K$, $\log(g) = 4.5$, [Fe/H] $= +0.2$, and $\xi = 2\,km\,s^{-1}$. This gave $\gamma_{1i} = 0.4622$, $\gamma_{2i} = 0.1784$, $\gamma_{1J} = 0.2609$, and $\gamma_{2J} = 0.2469$. Before fitting the light curves, we applied a scaling factor to the per data point errors in the *J*- and *i*-band light curves, such that the out-of-transit data when compared to a flat line gave a $\chi_\nu^2$ of unity. This was to account for any underestimation of the errors. The following parameters were allowed to vary in the MCMC analysis: the period (*P*), the epoch of mid-transit ($T_0$), the planet-star radius

ratio ($R_P/R_\star$), the impact parameter ($b = a \cos(i)/R_\star$, where *i* is the inclination), and the semimajor axis in units of the stellar radius ($a/R_\star$). Note that the radius ratio was assumed to be the same in both the *J*- and *i*-band transit models. The orbit was assumed to be circular, hence the eccentricity (*e*) was fixed to zero. Three chains of $1 \times 10^6$ steps were run each time to check convergence, then combined after discarding the first 10 per cent of each chain (the burn-in length).

The dilution-corrected light curves and their combined best-fitting model are shown in Fig. 3, and the resulting best-fitting model parameters are listed in Table 6. Fig. 9 shows the extent of correlation between some of the more correlated model parameters in this analysis. The distributions are not perfectly Gaussian and result in slightly asymmetric errors for the 68.3 per cent confidence interval about the median. In order to propagate these errors into the calculation of absolute dimensions, we have symmetrized the errors by adopting the mean of the 68.3 per cent boundaries (the 15.85 and 84.15 per cent confidence limits) as the parameter value (rather than the median), and we then quote the 68.3 per cent confidence interval as the ±1σ errors. The full extent of the relatively large errors on the blending fractions was explored by running the MCMC analysis on light curves corrected with the ±1σ limits of the estimated blending fractions. The quoted errors and parameter values were derived using the distributions from all of these runs. The results of fitting the original, diluted light curves are also given in Table 6 for completeness.

### 5.1.1 *J*-band secondary eclipse limits

WTS-2 b orbits very close to its host star and receives a high level of incident radiation ($F_{inc} \sim 1.3 \times 10^9$ erg s$^{-1}$ cm$^{-2}$). Following the prescription of López-Morales & Seager (2007) and assuming that the atmosphere has a zero-albedo ($A_B = 0$) and instantaneously re-radiates the incident stellar flux (i.e. no advection, $f = 2/3$), the expected equilibrium temperature of the planet is $T_{eq} = 2000 \pm 100\,K$. Although this is not as high as the hottest hot Jupiters (e.g. KOI-13 b has $T_{eq} \sim 2900\,K$, Mislis & Hodgkin 2012), WTS-2 b is one of the hottest planets orbiting a K dwarf. Adopting this value as the maximum day-side temperature of the planet and approximating the spectra of the planet and star as blackbodies, we expect the observed secondary eclipse depth in the WTS *J*-band light curve to be ~0.63 mmag. This value is calculated using the dilution-corrected light-curve analysis and then adding back in the ~19 per cent contamination of the WTS *J*-band light curve by the additional red source in the aperture. The out-of-eclipse data in the WTS-2 b *J*-band light curve has an rms of ~4 mmag, and is the typical rms of the WTS *J*-band light curves at *J* = 13.9 mag. There are 88 data points
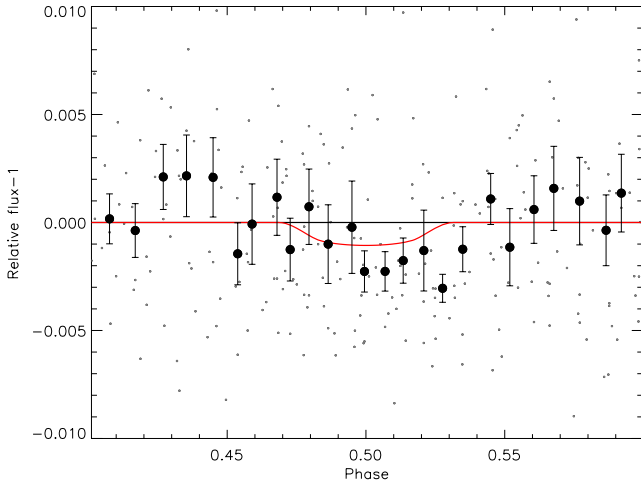
**Figure 10.** The observed WTS-2 b *J*-band light curve, i.e. without correction for dilution, zoomed around the expected secondary eclipse phase. The observed data are shown in grey dots, while the black filled circles are the data binned in phase with uncertainties equal to the standard error on the mean. The black solid horizontal line shows a flat model, i.e. no secondary eclipse detection. The solid red line is the best-fitting model light curve from a basic linear regression analysis, which gave a depth of $(F_P/F_\star) = 0.93 \times 10^{-3} \pm 0.69 \times 10^{-3}$, i.e. a non-detection. The model was fitted to data between phases $0.4 < \phi < 0.6$.

in the expected secondary eclipse of the WTS-2 b *J*-band light curve (according to the best-fitting model). Assuming white-noise only, this would result in a precision of ∼0.43 mmag on the secondary eclipse depth. We performed a basic linear regression fit to the WTS-2 *J*-band light curve with a model from the Mandel & Agol (2002) routines to attempt to detect the secondary eclipse of WTS-2 b. The best-fitting model is shown in Fig. 10 and corresponds to a flux ratio of $(F_P/F_\star) = 0.93 \times 10^{-3} \pm 0.69 \times 10^{-3}$. The large uncertainty is unsurprising and means that the WTS survey light curve is not capable of detecting the secondary eclipse, hence we are unable to constrain the properties of the planet's day side from the WTS data. The sparse sampling of the eclipse in the WTS light curve and the randomized observing pattern of the survey over many nights make it difficult to monitor the systematic effects during a single eclipse, hindering a robust measurement of the flux ratio. However, we do note that we find no evidence for an anomalously deep event, which supports the planetary nature of WTS-2 b. A single dedicated night of observation would in principle be able to measure the eclipse depth to a sufficient precision. The potential for follow-up studies of the planet's atmosphere is discussed in Section 7.4.

### 5.2 Radial velocity analysis

The RV curve has been modelled with constraints from the light-curve fit, rather than being fitted simultaneously with the light-curve data, due to the limited amount of RV data. To fit the RV curve, we adopted the well-defined period and transit ephemeris from the light curves and fixed these parameters in the RV curve model. We also fixed the orbit to be circular as we do not have enough data to model an eccentric orbit. Furthermore, a circular orbit is arguably the most reasonable approximation for a planet so close to its host star (see e.g. Anderson et al. 2012). The model takes the form of:

$$\mathrm{RV} = V_{\mathrm{sys}} + K_\star \sin(2\pi\phi) \qquad (1)$$

where $\phi$ is the phase, $K_\star$ is the RV semi-amplitude, and $V_{\mathrm{sys}}$ is the systemic velocity of the WTS-2 system. The phase-folded RVs and

the best-fitting model are plotted in Fig. 5, while Table 6 gives the resulting model parameter values. In the fit, the RV error bars have been scaled by $\sqrt{(\chi_\nu^2)} = 1.32$ such that $\chi_\nu^2 = 1$. This accounts for possible underestimation of the RV errors, or conversely, reflects the quality of the fit, and acts to enlarge the uncertainties on the model parameters, which are the $1\sigma$ errors from the $\chi^2$ fit. The best-fitting model gives a planet mass of $1.12 \pm 0.16 M_J$, where the error is calculated by propagating the errors of the relevant observables ($K_\star$, $M_\star$, $P$, and $i$).

## 6 ELIMINATING FALSE POSITIVES

Wide-field transit surveys invariably suffer from transit mimics, usually caused by eclipsing binaries, either as grazing systems, or by eclipsing binaries contaminated by a source of third light. Given that WTS-2 b is a relatively unusual planetary system, and the presence of a faint third light source in our aperture, it is important to investigate viable false-positive scenarios.

### 6.1 Non-blended false positives

Due to the faintness of our target, before proceeding to precision RV measurements with the 9.2-m HET, we carried out reconnaissance intermediate-resolution spectroscopy with the 3.5-m telescope at CAHA to check for large RV variations indicative of non-blended false positives such as a grazing binary, or a binary containing two identical size stars whose light curve has been erroneously phase folded on half of the true orbital period. The CAHA spectra were single lined, with no evidence for a double-peak in the cross-correlation functions, indicating that the system was not a non-blended false positive. Such scenarios would also have been reflected in the stellar density measured from the transit shape, as the density depends strongly on $P^{-2}$ (Seager & Mallén-Ornelas 2003). The measured RVs, given in Table 4, had an rms of 1.1 km s$^{-1}$ and were consistent with no significant RV variation within the precision of the measurements, ruling out companion masses $>5M_J$ for non-blended scenarios.

### 6.2 Blended false positives

Despite the orders of magnitude larger RV variations expected for a binary system, in the case where the binary spectral lines are blended with a brighter foreground star, the overall variations in the cross-correlation profile can have significantly smaller amplitudes, potentially as small as that expected for a giant planet. Such a system would produce significant line-profile variations, so we measured the bisector spans (i.e. the difference between the bisector values at the top and at the bottom of the correlation function; Torres et al. 2005) for each epoch of high-resolution HET spectra. In the case of contamination from a blended binary, or stellar atmospheric oscillations, we would expect to measure bisector spans values consistently different from zero, and as a strong function of the measured RVs (Queloz et al. 2001; Mandushev et al. 2005). Fig. 11 shows the measured bisector spans as a function of phase and RV. Although the bisector span values are scattered around zero, they have large errors and an rms scatter (∼1 km s$^{-1}$) that exceeds the measured RV semi-amplitude (0.256 km s$^{-1}$). The result is that they are too noisy to conclusively rule out any blended eclipsing binary scenario.

Instead, to further rule out blended eclipsing binary scenarios, we consider the following information. First, the transit depths in the *i* and *J* bands are very consistent. Thus, if the light curves were
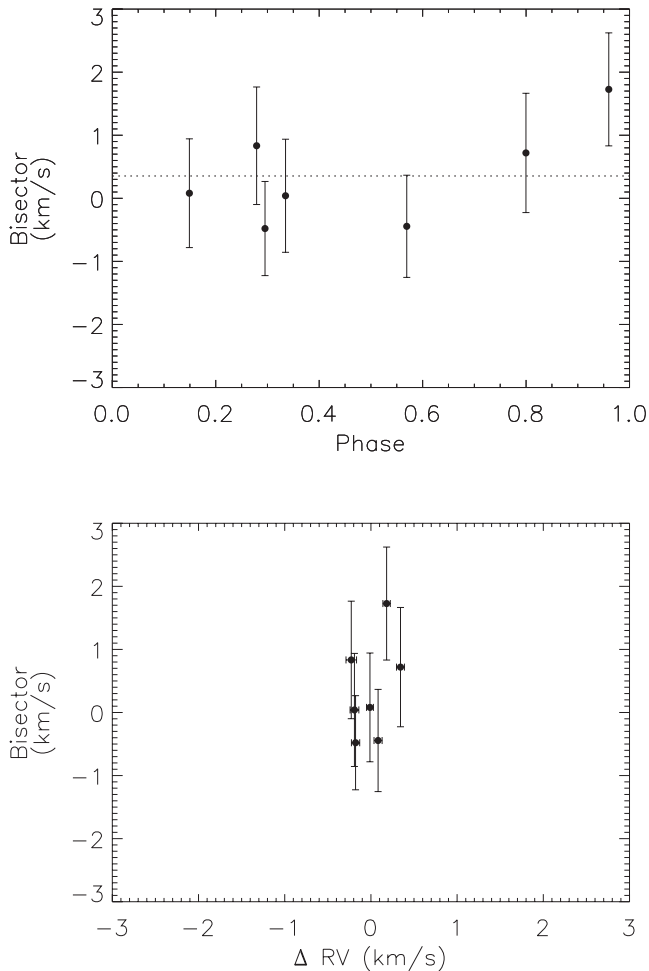
**Figure 11.** Bisector spans for WTS-2 b measured from high-resolution HET spectra, as a function of phase and as a function of the change in RV. Due to the large errors on the bisectors, we cannot use them to assess the possibility of a blending eclipsing binary in the aperture and instead use other methods detailed in this section.

generated by a background eclipsing binary blended with a bright foreground K dwarf, then the colour (i.e. surface temperature) of the eclipsed star should also be similar to a K dwarf. Secondly, the mean stellar density derived from the best-fitting transit model is in excellent agreement with the stellar density inferred from spectroscopic observations of the brightest source in the aperture, i.e. a K dwarf. Again, this implies that the eclipsed star should be similar in nature to the spectroscopically observed K dwarf. Now, if we assume a significant fraction of the light in the observed light curves originates from the foreground K dwarf and subtract it, we find that the transit can no longer be fitted by a K-dwarf star, instead requiring a cooler, denser star to fit the transit shape, which is in contradiction to our first two statements. This already indicates that a blended eclipsing binary scenario can be rejected but it is important to robustly rule out the detected red object within the aperture as the source of the occultations.

To further explore the role of additional light in the observed light curves, we use constraints provided by a simultaneous modelling of the *i*- and *J*-band light curves. Following a similar method outlined by Snellen et al. (2009) and Koppenhoefer et al. (2013) for assessing the blend scenarios for OGLE-TR-L9 b and POTS-1 b, we simulate background eclipsing binary systems blended by different amounts

of light from a third star using the Mandel & Agol (2002) algorithms. This analysis was carried out on the observed light curves, i.e. the light curves that have not been corrected for the known amount of dilution by the faint red source identified by AstraLux imaging (see Section 3.5), and can thus be considered an independent test of the blending fraction.

In the simulations, we vary two parameters: (i) the difference in surface temperature between the eclipsed star and the blending source, $\Delta T$, and (ii) the fraction of light from the blending source $(0 < F_{3rd} < 90$ per cent). The combined light should produce a spectrum with a temperature that matches the spectroscopic measurement, i.e. 5000 K. Any small fraction of light originating from the eclipsing star is included in $F_{3rd}$. We exclude models which give stellar densities inconsistent with stellar evolutionary tracks, although we allow any evolutionary status for the eclipsed star since we do not insist that the contaminant is bound to the observed K dwarf, even though this is quite likely (see Section 3.5). Fig. 12 shows the upper limits on the allowed eclipsed star density across a range of masses based on the Siess et al. (2000) evolutionary tracks. For each combination of $F_{3rd}$ and $\Delta T$, we allow the binary radius ratio and the impact parameter to vary freely in the simulation, while the density of the eclipsed star is limited to be below the maximum density allowed based on the temperature of the eclipsed star ($T_{ecl}$). The fractional contribution of the light from the third star is also adjusted in each waveband based on blackbody spectra. Given that we are most concerned about blends with a background eclipsing M dwarf, we set the limb-darkening coefficients to be appropriate for a 3500 K eclipsed star throughout. Although this is not strictly valid for hotter models, the effect of the limb darkening is marginal compared to the large chromatic variations caused by observing in different filters.

The bottom panel of Fig. 12 shows the $\chi^2$ confidence contours of fitting blended transit models to the two light curves simultaneously. $\Delta T = 0$ K corresponds to $T_{ecl} = T_{3rd} = 5000$ K, while $F_{3rd}$ refers to the fraction of blending light in the *i* band. It shows that the data can only be well fitted by a low level of blending light from a source that is redder than the occulted star. In fact, the preferred solution is for a blending fraction of ∼10 per cent by an object of $T_{3rd} \sim 3600$ K. This matches extremely well with the independent measurement of the blended light fraction from the AstraLux imaging (see Section 3.5). If the observed light curve had been generated by a foreground K-dwarf diluting eclipses from a background M-dwarf eclipsing binary, the simulations would have congregated in the upper-left corner of the plot. However, these models produce transit shapes that are too wide, too V shaped or too colour dependent to match the data.

Finally, we note that it is unlikely that star spots are responsible for the RV variations as a ∼1-d period would correspond to a rotational velocity of ∼40 km s$^{-1}$ for a K2V star, which is inconsistent with our measured $v \sin i$ unless there is a high degree of spin–orbit axis misalignment, which seems to be unlikely for cool dwarfs (Winn et al. 2010).

All of these factors combined lead us to conclude that the planetary nature of the detected system is robust, despite that lack of a conclusive bisector span analysis.

# 7 DISCUSSION

We have presented WTS-2 b, the second planet to have been discovered in the infrared light curves of the WTS. The notable property of this otherwise typical hot Jupiter is its orbital separation of just $a = 0.01855$ au, which places the planet in the small but

**Figure 13.** The distribution of $a/a_{\text{Roche}}$ as a function of stellar mass for all known transiting exoplanets. WTS-2 b is marked by the red filled square and is one of the closest exoplanets to the separation at which it would begin to lose mass. A few other systems of note are labelled. The horizontal dashed line marks the ideal circularization radius (Ford & Rasio 2006), i.e. where highly eccentric orbits caused by e.g. planet–planet scattering are circularized. Data from exoplanets.org.

growing sample of extreme giant planets in sub-0.02 au orbits. The planet's orbit is just 1.5 times the tidal destruction radius, i.e. the critical separation inside which the planet would to lose mass via Roche lobe overflow, $a_{\text{Roche}} \approx 2.16 R_P (M_\star/M_P)^{1/3}$ (Faber, Rasio & Willems 2005; Ford & Rasio 2006). Fig. 13 shows the distribution of $a/a_{\text{Roche}}$ as a function of stellar mass for transiting exoplanets, marking WTS-2 b as one of the closest systems to tidal destruction, particularly for low-mass host stars. Throughout this discussion, we use parameter values for WTS-2 b derived from the analysis of the dilution-corrected light curve (see Section 5.1).

### 7.1 Remaining lifetime

The close proximity of WTS-2b to its host star suggests that its orbital evolution is dominated by tidal forces (e.g. Rasio & Ford 1996; Pätzold & Rauer 2002). The tide raised on the star by the planet exerts a strong torque that transfers the angular momentum of the planetary orbit to the stellar spin (e.g. Goldreich & Soter 1966; Zahn 1977; Hut 1981; Eggleton, Kiseleva & Hut 1998), causing the planet to spiral inwards and the star to spin up. In our case, the tide raised on the planet by the star is ignored as we have (reasonably) assumed that the planet is on a circular orbit and synchronized. Following Matsumura, Peale & Rasio (2010), we find that the total angular momentum, $L_{\text{tot}}$, in the WTS-2 b system compared to the critical angular momentum, $L_{\text{crit}}$, required for the star–planet system to reach a state of tidal equilibrium, i.e. dual synchronization, is $L_{\text{tot}}/L_{\text{crit}} \sim 0.57$ which is $< 1$, indicating that WTS-2 b will never reach a stable orbit and will continue to spiral in towards the host star under tidal forces until it is inside $a_{\text{Roche}}$, where it will presumably be destroyed by Roche lobe overflow (Gu, Lin & Bodenheimer 2003). First, let us estimate how long will it take before the planet meets its demise and if the orbital decay will be directly observable on the decade time-scale, according to the standard $Q'_\star = 10^6$ calibration.

To estimate the remaining lifetime of WTS-2 b, we take a simple model of tidal interactions, namely the damping of the equilibrium tide by viscous forces inside the star, i.e. the hydrostatic adjustment



**Figure 12.** Top: stellar evolutionary tracks showing the variation in mean stellar density with stellar surface temperature for a range of ages and masses, based on the Siess, Dufour & Forestini (2000) models. The dashed line marks the maximum possible density for a given surface temperature. The horizontal dotted line marks the stellar density measured from the best-fitting model to the dilution-corrected light curves. Bottom: confidence intervals from the simultaneous $\chi^2$ analysis of all possible blended eclipsing binary scenarios fitted to the i- and J-band light curves. The y-axis gives the blended light fraction for the i band and the x-axis gives the difference in surface temperature between the eclipsed star and the third light star. The combined light curves significantly favour a low level of blending by a source that is redder than the main contributor of light in the aperture. Note that blended background M-dwarf eclipsing binaries solutions lie in the upper left of this plot and are very poor fits to the light curves in the two different bandpasses.

of the star to the imposed gravitational field of the planet, with the tidal bulge lagging the planet by a constant time (Hut 1981; Eggleton et al. 1998). Note that we chose this model as it has been shown by Socrates & Katz (2012) that the constant time lag model has a better physical motivation than the constant phase lag model (Goldreich & Soter 1966), as it is independent of the orbital configuration. In this model, the rate of semimajor axis decay is given by (Matsumura et al. 2010)

$$\frac{\dot{a}}{a} = -6k_2\Delta t \frac{M_P}{M_\star}\left(\frac{R_\star}{a}\right)^5 n^2, \tag{2}$$

under the simplifying assumptions that the relevant tidal frequency is simply the planet's mean motion ($n = 2\pi/P$), the orbit is circular ($e = 0$), the planet rotation is synchronized with the orbit, and that the star is non-rotating. Here, $k_2$ is the star's second-order Love number (related to the star's density profile) and $\Delta t$ is the constant time lag. In this model, assuming that the planet does not change the star's spin significantly, integrating equation (2) gives the future lifetime

$$t_{\text{life}} = -\frac{a^8}{48k_2\Delta t\, G M_P R_\star^5}. \tag{3}$$

Note that $t_{\text{life}}$ is the time until $a = 0$ au, but that the difference in time between this and $a = a_{\text{Roche}}$ is negligible. As mentioned previously, the strength of tidal forces is commonly parametrized by means of the tidal quality factor $Q'_\star$, with a higher $Q'_\star$ meaning weaker tidal dissipation. While in the highly simplified constant phase lag model (Goldreich & Soter 1966) $Q'_\star$ is a constant, this is not in general true. In our adopted constant time lag model, $Q'_\star$ is related to the lag time by (Matsumura et al. 2010)

$$Q'_\star = \frac{3}{4k_2\Delta t n}. \tag{4}$$

Adopting $Q'_\star = 10^6$ for the current-day WTS-2 b system, based on previous studies of $Q'_\star$ (Trilling et al. 1998; Meibom & Mathieu 2005; Jackson et al. 2008), we find a remaining lifetime of $\sim$40 Myr, which is just 7 per cent of the youngest possible age of the system ($\gtrsim$600 Myr), and <1 per cent for the more typical older field star ages allowed by the stellar model isochrones used in Section 4.2. Two situations arise from this, either (i) the system is undergoing a rapid orbital decay and is genuinely close to destruction, in which case we can measure the tidal decay directly by monitoring the transit time shift over tens of years, or (ii) $Q'_\star$ is larger so that the system decays more slowly, or has a more complicated dependency on other system parameters.

## 7.2 Transit arrival time shift

In the case of scenario (i), we can calculate how long it would take to observe a significant shift in the transit arrival time of WTS-2 b. For this, we need to know the current rate of orbital angular frequency change ($dn/dt$), which can be calculated via the chain rule using equation (2) and the derivative of Kepler's third law in terms of $n$ with respect to $a$ (i.e. $dn/da$):

$$\frac{dn}{dt} = \left(\frac{dn}{da}\right)\dot{a} = -\left(\frac{27}{4}\right)n^2\left(\frac{M_P}{M_\star}\right)\left(\frac{R_\star}{a}\right)^5\left(\frac{1}{Q'_\star}\right), \tag{5}$$

For WTS-2 b, assuming $Q'_\star = 10^6$, we find that $dn/dt = 1.059\,4599 \times 10^{-20}$ rad s$^{-2}$. To calculate the expected transit time shift, $T_{\text{shift}}$, after a time $T$, we note that the angle $\theta$ swept out by a planet orbiting with angular frequency $n = d\theta/dT$ increasing at a constant rate of $dn/dT$ is, via Taylor expansion:

$$\theta = n_0 T + \frac{1}{2}T^2\left(\frac{dn}{dT}\right). \tag{6}$$

The angular difference between the linear ephemeris and the quadratic ephemeris after $T$ years is simply the quadratic term, thus the transit arrival time shift is

$$T_{\text{shift}} = \frac{1}{2}T^2\left(\frac{dn}{dT}\right)\left(\frac{P}{2\pi}\right), \tag{7}$$

where $P$ is the orbital period. Note that equations (5) and (7) carry the same assumptions as equation (2). Assuming that current instrumentation can reach a timing accuracy of 5 s (see e.g. Gillon et al. 2009), the decay of WTS-2 b's orbit would be detectable after $\sim$15 yr ($T_{\text{shift}} \sim 17$ s for $Q'_\star = 10^6$), but it remains the best target to observe this phenomenon for early to mid K-dwarf host stars. If no detectable transit time shift is found in the WTS-2 b system, it provides a stringent lower limit for the value of $Q'_\star$ in the sparsely sampled K-dwarf regime, thus helping to constrain tidal evolution theories that argue $Q'_\star$ is dependent on the depth and mass of the convective outer envelope of the host star (Barker & Ogilvie 2009, 2010; Penev & Sasselov 2011).

We have predicted the $T_{\text{shift}}$ values for a sample of known transiting hot Jupiters ($M_P > 0.3M_J$) to determine if direct observational constraints across the entire mass range of planet host stars are achievable within a decade. Such constraints could be used to address the dependence of $Q'_\star$ on the depth of the stellar convective envelope. The sample was selected from the exoplanets.org data base, choosing systems with approximately circular orbits ($e < 0.01$), and contains 101 planets (as of 2014 January 20). We assume these hot Jupiter systems contain only one planet and do not have stellar companions, such that additional transit timing variations can be ignored. Choosing near circular orbit systems also allows us to neglect issues such as precession of the orbit, the stellar oblateness, and the value of the planetary tidal quality factor (although these effects are likely to be small). For these reasons, the well-known close-in hot Jupiter WASP-12 b is excluded from our sample, owing to its stellar and planetary companions, and slightly eccentric orbit (Husnoo et al. 2011; Bergfors et al. 2013; Maciejewski et al. 2013). The left-hand panel of Fig. 14 shows our predicted $T_{\text{shift}}$ values for the sample after 10 yr as a function of stellar host mass assuming $Q'_\star = 10^6$ in equation (5). There are a number of systems with feasibly observable variations in their transit arrival time whose host stars span a variety of stellar internal structures and could provide direct observational constraints on $Q'_\star$ within a decade with current instrumentation. The right-hand panel of Fig. 14 depicts how long one would need to wait in order to place a lower limit constraint on $Q'_\star$ in our adopted model for some of the most perturbed systems, e.g. after 25 yr, if no detectable transit time shift is observed, one could rule out values of $Q'_\star < 1 \times 10^7$ across a wide range of stellar masses. Note however that future transit arrival time shift measurements require similarly accurate measurements of the planets' current-day periods and ephemerides. Intriguingly, tentative measurements of period decay rates in WASP-43 b and OGLE-TR-113 b for example, which orbit M- and K-dwarf host stars, suggest relatively small values of $Q'_\star$, of the order of $10^3$–$10^4$; however, further data over several years is required to confirm these results (Adams et al. 2010; Blecic et al. 2013; Murgas et al. 2014).
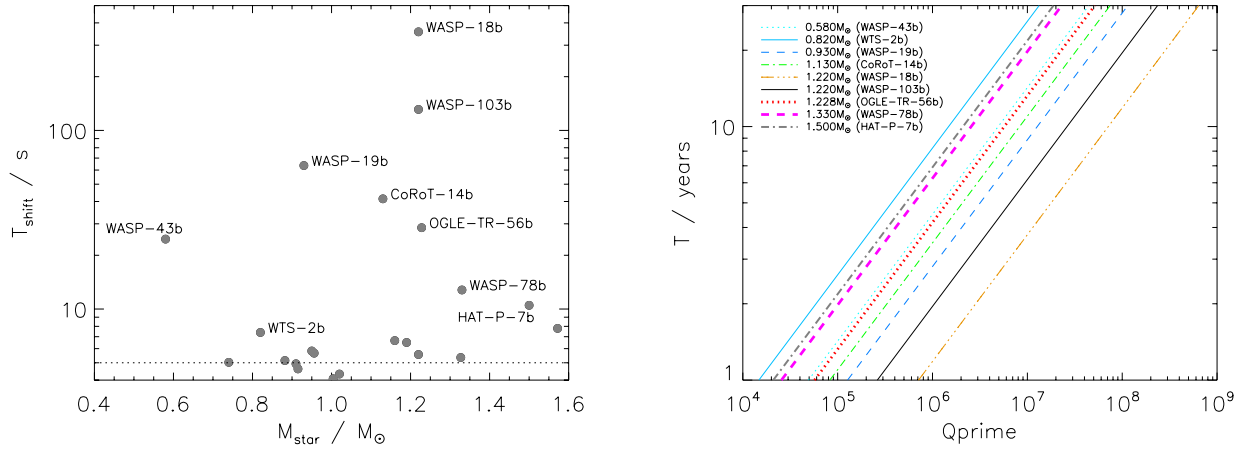
**Figure 14.** Left: transit time shifts after 10 yr for known transiting hot Jupiters assuming $Q'_\star = 10^6$ in equation (5). The more significantly shifted planets are labelled. The horizontal dotted line marks the 5 s timing accuracy possible with current instrumentation. After 10 yr, strong observational constraints on $Q'_\star$ would be available across the full stellar mass range of exoplanets host stars. Right: the amount of time after discovery one would need to wait to detect $T_{\text{shift}} = 5$ s for a given $Q'_\star$, e.g. after $T \sim 25$ yr, one could rule out $Q'_\star \leq 10^7$ across a range of stellar masses if no detectable shift was observed.

### 7.2.1 WASP-18 b

Importantly, we note here that for the most extreme planet, WASP-18 b, equations (5) and (7) give $\mathrm{d}n/\mathrm{d}t = 5.53 \times 10^{-19}$ rad s$^{-2}$ (which corresponds to a rate of change of period of $\mathrm{d}P/\mathrm{d}t = -0.018$ s yr$^{-1}$) and a corresponding $T_{\text{shift}} \sim 356$ s after 10 yr for $Q'_\star = 10^6$, which is significantly more than the predicted $T_{\text{shift}} = 28$ s reported in Hellier et al. (2009). There are several differences between our methods of calculating $T_{\text{shift}}$ and the WASP-18 b discovery paper, for example, Hellier et al. (2009) used the tidal evolution formalism of Dobbs-Dixon, Lin & Mardling (2004), which defines $Q'_\star$ to be a factor of 2 different to our adopted formalism, and they also included the effects of stellar rotation and the stellar wind which we have neglected here. However, none of these factors are sufficient to explain the order of magnitude difference between the predicted $T_{\text{shift}}$ values for WASP-18 b. We also note that a $T_{\text{shift}}$ of the order of hundreds of seconds for WASP-18 b is consistent with scaling the theoretical calculations of Penev & Sasselov (2011) for $Q'_\star = 10^6$. Given that our equations give a similar remaining lifetime for WASP-18 b ($\sim$0.72 Myr) to that reported by Hellier et al. (0.65 Myr), our orbital evolution tracks and in-spiral times appear to agree. We have therefore concluded that a simple numerical error occurred in the WASP-18 b discovery paper at the final stage of converting the orbital evolution into $\mathrm{d}P/\mathrm{d}t$ and a corresponding transit arrival time shift (Collier Cameron, private communication), and that under the assumption of $Q'_\star = 10^6$, observable shifts in the transit timing of WASP-18 will arrive much earlier than previously thought. In fact, we calculate that a shift of 28 s for the WASP-18 b transit would only take $\sim$3 yr, which is a positive outcome. Maxted et al. (2013) found no evidence for variations in the times of transit from a linear ephemeris for WASP-18 b greater than 100 s after 3 yr, but if $Q'_\star$ is genuinely close to $10^6$, we expect to see evidence of this much sooner than a decade. We also note that our predicted timing variation for WASP-18 b over 10 yr is now much larger than that predicted to be caused by the Applegate effect on similar time-scales (Watson & Marsh 2010).

### 7.3 Current observational constraints on $Q'_\star$

Rather than waiting to observe a decaying orbital period by measuring transit arrival time shifts, can we already rule out low values

of $Q'_\star$ ($\lesssim 10^6$)? For example, in the individual case of WASP-19 b, Hellier et al. (2009) suggest $Q'_\star \sim 10^7$, else the probability of observing the planet in its current evolutionary state is unlikely given the known population of hot Jupiters. However, the growing number of very close-in hot Jupiters suggests that the population should be treated as whole. Penev et al. (2012) performed a population study of transiting exoplanets in circular orbits around stars with surface convective zones, to find a $Q'_\star$ that would give a statistically likely distribution of remaining planet lifetimes. They assumed that the orbits of the planets initially evolved only under gas disc migration and then by tidal forces alone since the zero-age main sequence. They integrated the orbital evolution from 5 Myr based on the given ages of its host star, and argued that $Q'_\star \gtrsim 10^7$ in order to fit the observed population at the 99 per cent confidence level. Their largest source of uncertainty was the error on the stellar ages, but even accounting for this they still found inconsistent with low values of $Q'_\star$. However, Penev et al. (2012) point out that their result may not be valid for other giant planet migration mechanisms, such as dynamical scattering, and that their model is not valid for stars without surface convective layers so they excluded any host star with $M_\star > 1.25\,\mathrm{M}_\odot$, which could be subject to a different mode of tidal dissipation. We also note that high values of $Q'_\star$ for those planets deposited close to the host star before the dispersal of the gas disc ($\lesssim$10 Myr; Hernández et al. 2007; Wyatt 2008) are perhaps expected as the tidal migration would need to be slow over the host star's main-sequence lifetime.

Here, we attempt a complementary study to that of Penev et al. (2012), in that we assume that the population of hot Jupiters instead migrated by scattering on to eccentric orbits (it is interesting to note here that the likely bound M dwarf at 0.6 arcsec separation from WTS-2 is a potential source of Kozai perturbations which could also trigger the migration of the gas giant). Planets scattered such that their eccentric orbit just grazes $a = a_{\text{Roche}}$ are tidally circularized to $2a_{\text{Roche}}$ (Ford & Rasio 2006; Nagasawa, Ida & Bessho 2008), and we assume that any inside $2a_{\text{Roche}}$ at present day are assumed to have migrated under tidal forces alone from there (see Fig. 13). The key difference is that we assume the scattering event can occur at any point during the planet's total lifetime so the tidal forces have not necessarily been dominant during the majority of the planet's lifetime. This assumption means that the pile-up of planets near $2a_{\text{Roche}}$ is constantly replenished. If planets are continuously
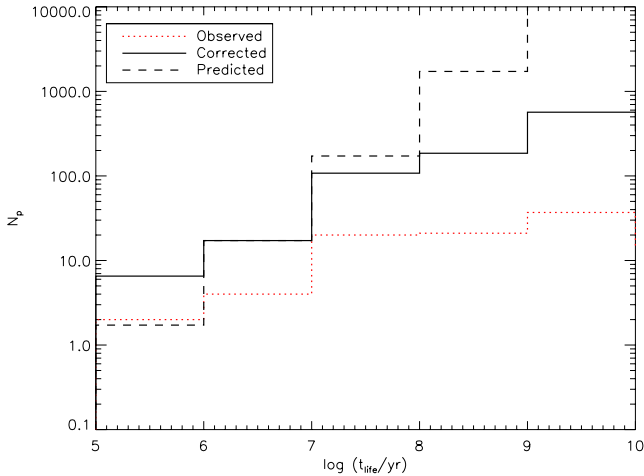
**Figure 15.** Histogram of the calculated remaining lifetimes of observed systems (red dotted line) using $Q'_\star = 10^6$. The black solid line histogram shows the distribution after a correction for transit probability and survey completeness. The dashed black line shows the distribution we expect to observe if planets are falling in under tidal forces at a constant rate in time, using $Q'_\star = 10^6$. The predicted distribution is scaled using the 1–10 Myr bin which we have assumed is the least affected by incompleteness. The corrected and predicted distributions are discrepant at long remaining lifetimes, implying that our model of the tidal forces is incorrect, but the survey completeness correction makes these bins uncertain (see Section 7.3).

falling in from the pile-up at a constant rate in time due to tidal forces, then our model given in equation (2) will give a distribution of remaining lifetimes that is uniformly distributed in time. For example, for every one planet we see with a remaining lifetime of 0.1−1 Myr, we expect to see 10 with remaining lifetimes of 1−10 Myr, 100 with remaining lifetimes of 10−100 Myr, and so on. If the calculated remaining lifetime distribution for the observed population diverges from this, our model and adopted value of $Q'_\star = 10^6$ are not observationally supported. However, if the distribution matches, planets such as WASP-18 b and WASP-19 b are consistent with being genuinely close to destruction and their detection is not so unlikely. For simplicity, we have used the sample of hot Jupiters that we created in Section 7.2. Due to the dependence of $Q'_\star$ on the orbital period, we assign a current-day $Q'_\star$ to each system by assuming that it had $Q'_\star = 10^6$ at its 3 d orbital separation. This ensures that $\Delta t$ in equation (3) is constant for all systems, allowing a physically meaningful comparison between planets.

The resulting distribution of observed remaining lifetimes is shown as a red dotted-line histogram in Fig. 15. We correct the observed distribution of remaining lifetimes to account for the geometrical alignment bias in the transit detection probability, such that each planet observed is representative of a population of $\sim (a/R_\star)$ planets. We also correct for survey incompleteness using the detection probability function described by Penev et al. (2012), which is 100 per cent complete out to 2 d and tails off at longer periods. Applying these corrections yields the histogram shown by the solid black line in Fig. 15. The predicted distribution (dashed line), i.e. that which increases by a factor of 10 for each bin, is created by scaling to the 1−10 Myr bin. This bin was chosen for the scaling as it has the best combination of sample size and completeness. In the longest remaining lifetime bins, the bias-corrected distribution is highly discrepant with the predicted one, suggesting that either $Q'_\star$ is indeed higher, so that planets do not typically spiral into their hosts within the age of the system, or that $Q'_\star$ may have a complicated frequency dependence making the future lifetime of the

system hard to predict. The latter possibility is predicted by various dynamical tide mechanisms, i.e. the excitation of normal modes in the star by the imposed gravitational field (see e.g. Ogilvie & Lin 2007), with the tidal quality factor varying by orders of magnitude with small changes in the planet's orbital frequency as different modes are excited in the star. In this case, the planets with supposedly short lifetimes could be temporarily stuck in a region of high $Q'_\star$ after migrating rapidly from a feeding region where $Q'_\star$ is lower. A third possibility is that mass-loss as the planet's size approaches its Roche lobe causes orbit expansion that retards the tidal decay (Fossati et al. 2010; Li et al. 2010; Haswell et al. 2012). However, using the equations of Li et al. (2010), we estimate that at least in the case of WTS-2b such mass-loss is negligible, around $10^4$ times less than that for WASP-12b.

However, the simplifications in our population study bias us against longer remaining lifetimes, i.e. we have excluded eccentric systems which tend to have longer periods, and we do not have a detailed treatment of the long-period sensitivity of the transit surveys contributing to the sample. While RV surveys suggest that it is unlikely that the number of longer lifetime (longer period) systems will increase dramatically, our bias-corrected distribution of remaining lifetimes is still uncertain, and it is not straightforward to reconstruct it.

Although more detailed population studies, such as that by Penev et al. (2012), strongly advocate $Q'_\star \gtrsim 10^7$ for the general population of exoplanets, this is under one specific set of initial conditions (e.g. gas disc migration) with some idealized assumptions about the chances of a planet candidate being confirmed by follow-up considering the human element involved in its assessment and the availability of resources. Such studies will always be hampered by these uncertainties and while they provide some generalized constraints on $Q'_\star$, we conclude that the most informative and straightforward constraints on $Q'_\star$ are best obtained through the monitoring of orbital periods in individual close-in giant planet systems. Even in the case of no detectable period decay, this places a constraint on the rate of change of orbital period, and hence definitive limits on the value of $Q'_\star$. Importantly, each system acts as a probe of different parameters that $Q'_\star$ may be dependent on e.g. the internal structure of the host star, such that even a relatively small sample of planets can lead to strong observational constraints $Q'_\star$ (see right-hand panel of Fig. 14). To achieve the same results with population studies, i.e. studying $Q'_\star$ as a function of host star mass, would require many more well-characterized systems per host star mass bin, and although future space-based and ground-based planet discovery missions may provide this, it is likely to be on a similar time-scale to the technological advancements in precision timing measurements. Consequently, we find that monitoring changes in orbital periods of close-in giant planets will be the most informative and least assumption-prone method for observationally constraining $Q'_\star$.

### 7.4 Follow-up potential

In terms of planetary mass and host star, WTS-2 b is very similar to the well-known hot Jupiter HD 189733 b (Bouchy et al. 2005). However, WTS-2 b receives almost three times as much incident stellar radiation on account of its closer orbit, resulting in an expected maximum day-side temperature that is ~500 K hotter than HD 189733 b. Stellar irradiation is expected to be a dominant factor in determining the atmospheric properties of a hot Jupiter (e.g. Fortney et al. 2008). From this, WTS-2 b is expected to have an inversion layer (stratosphere) in its atmosphere, caused by gaseous absorbing com-
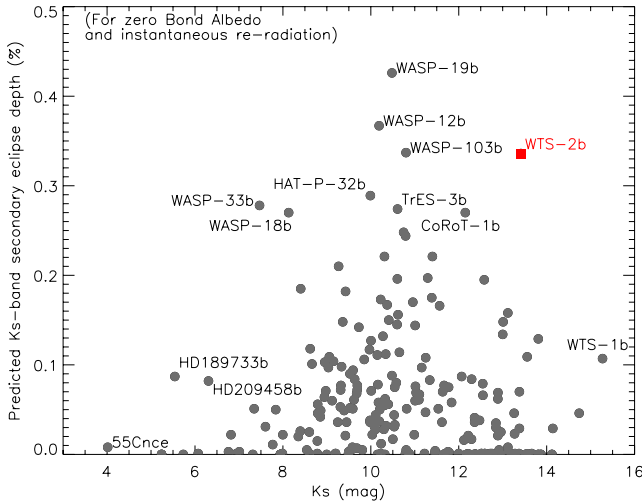
**Figure 16.** Expected $K_s$-band secondary eclipse depths for the currently known exoplanets as a function of the system's $K_s$-band magnitude. Eclipse depths are calculated assuming the maximum day-side temperature ($A_B = 0$, $f = 2/3$, i.e. no advection of energy from the day-side to the night-side) for all planets. WTS-2 is marked by the red square and is one of the deepest predicted $Ks$-band secondary eclipse depths, making it more favourable for ground-based atmospheric characterization studies. Note that these are not measurements and that the true depth can deviate e.g. HD189733 b 0.039 per cent (Swain et al. 2009). Also note that WTS-2 b is the expected depth without adding in contamination from the red companion, and will depend on the spatial resolution of the observations. Planet and stellar data from exoplanets.org 20/01/2014.

pounds (Burrows, Budaj & Hubeny 2008). In cooler atmospheres, these absorbers condense out, as may be the case for HD189733 b, which does not exhibit an inversion layer (Charbonneau et al. 2008; Birkby et al. 2013). Multiwavelength measurements of the WTS-2 b secondary eclipse depth will allow the temperature structure of its atmosphere to be determined. The fact that WTS-2 b is very hot and orbits a relatively small star means that its secondary eclipse depths will be deeper compared to other hot Jupiters of similar $T_{eq}$ orbiting more luminous stars. To assess the potential of ground-based follow-up studies of WTS-2 b's atmosphere, we have calculated the expected secondary eclipse depths for WTS-2 b at optical and infrared wavelengths again following the equations of López-Morales & Seager (2007). We approximate the stellar and planetary spectra as blackbodies, and assume the maximum day-side temperature for the planet $T_{eff, p} = 2000$ K, i.e. zero-albedo (no reflection) and no advection of incident energy from the day side to the night side. The expected planet/star flux ratios in the $I$, $Z$, $J$, $H$, and $K_s$ bandpasses, based on the dilution-corrected light-curve analysis, are $\sim 0.14 \times 10^{-3}$, $\sim 0.19 \times 10^{-3}$, $\sim 0.75 \times 10^{-3}$, $\sim 1.5 \times 10^{-3}$, and $\sim 2.6 \times 10^{-3}$, respectively. Note that any potential follow-up observations would need to add the expected contamination from the M-dwarf companion to these values. For example, if the M-dwarf is entirely contained within the photometric aperture, the expected observed depths would be $\sim 0.12 \times 10^{-3}$, $\sim 0.17 \times 10^{-3}$, $\sim 0.63 \times 10^{-3}$, $\sim 1.25 \times 10^{-3}$, and $\sim 2.12 \times 10^{-3}$, in the $I$, $Z$, $J$, $H$, and $K_s$ bandpasses, respectively.

Figure 16 shows the expected non-contaminated $K_s$-band secondary eclipse depth of WTS-2 b in the context of other transiting exoplanets, again assuming that each planet has $A_B = 0$ and $f = 2/3$. We find that WTS-2 b has one of the deepest predicted $K_s$-band secondary eclipses amongst the known exoplanet population. Although the host star is relatively faint, such a deep secondary eclipse

could potentially be detected with ground-based infrared facilities. For example, both the Long-slit Intermediate Resolution Infrared Spectrograph (LIRIS) at the 4-m William Herschel Telescope in La Palma, and WFCAM on UKIRT in Hawaii have a proven record for detecting such events (see e.g. Snellen & Covino 2007; de Mooij & Snellen 2009; de Mooij et al. 2011). It has also been shown that the presence of an inversion layer may depend on the activity of the host star, whereby UV flux from an active host star causes photodissociation of the absorbing compounds in the planet's upper atmosphere preventing the temperature inversion (Knutson, Howard & Isaacson 2010). A measurement of the activity level in the WTS-2 host star is not only a useful ageing diagnostic, but also key to understanding the planet's atmospheric properties. Measurements of the WTS-2b secondary eclipse would also help constrain the eccentricity of the system, and improve the ephemeris of the orbit, aiding future studies of orbital decay in the system.

# 8 CONCLUSIONS

We have reported the discovery of WTS-2 b, a typical transiting hot Jupiter in an unusually close orbit around a K2V star, which has a likely gravitationally bound M-dwarf companion at a projected separation of 0.6 arcsec. The proximity of the planet to its host star places it at just 1.5 times the separation at which it would be destroyed by Roche lobe overflow. The system provides a calibration point for theories describing the effect of tidal forces on the orbital evolution of giant planets, which are poorly constrained by observations. In particular, the system is useful for constraining theories that predict host stars with deeper convective envelopes leading to more efficient tidal dissipation. Using a simple model of tidal orbital evolution with a tidal dissipation quality factor $Q'_\star = 10^6$, we calculated a remaining lifetime for WTS-2 b of just 40 Myr. The decaying orbit corresponds to a shift in the transit arrival time of WTS-2 b of $\sim$17 s after 15 yr. We have also reported a correction to the previously published predicted shift in the transit arrival time of WASP-18 b, which used a very similar model for the stellar tides. We have calculated that the WASP-18 b transit time shift is 356 s after 10 yr for $Q'_\star = 10^6$, which is much larger than the previously reported 28 s. We found that transit arrival time measurements in individual systems could place stringent observational constraints on $Q'_\star$ across the full mass spectrum of exoplanet host stars within the next decade. Our attempt to constraint $Q'_\star$ via a study of the observed population of currently known transiting hot Jupiters was inconclusive, requiring a more detailed and precise determination of transit survey sensitivities at long periods. We conclude that the most informative and straightforward constraints on $Q'_\star$ and the theory of tidal orbital evolution for exoplanets will be provided by transit arrival time shifts in individual systems. Finally, WTS-2 b is one of the most highly irradiated gas giants orbiting a K dwarf and is therefore expected to have an inversion layer in its atmosphere. This is in contrast to the non-inverted atmosphere of HD 189733 b, which has a very similar planet mass and host star to WTS-2 b, but receives $\sim$3 times less incident radiation. Despite the relatively faint magnitude of the host star, the system size ratio and hot day-side temperature result in predicted infrared secondary eclipses that are within the reach of current ground-based instrumentation.

## REFERENCES

Adams E. R., López-Morales M., Elliot J. L., Seager S., Osip D. J., 2010, ApJ, 721, 1829

Aigrain S., Irwin M., 2004, MNRAS, 350, 331

Anderson D. R. et al., 2012, MNRAS, 422, 1988

Baraffe I., Chabrier G., Allard F., Hauschildt P. H., 1998, A&A, 337, 403

Barbuy B., Perrin M.-N., Katz D., Coelho P., Cayrel R., Spite M., Van't Veer-Menneret C., 2003, A&A, 404, 661

Barker A. J., Ogilvie G. I., 2009, MNRAS, 395, 2268

Barker A. J., Ogilvie G. I., 2010, MNRAS, 404, 1849

Barnes S. A., 2007, ApJ, 669, 1167

Batalha N. M., Borucki W., Caldwell D. A., Chandrasekaran H., Gautier T. N., Jenkins J., Koch D. G., 2006, BASS, 38, 210.08

Bayo A., Rodrigo C., Barrado Y Navascués D., Solano E., Gutiérrez R., Morales-Calderón M., Allard F., 2008, A&A, 492, 277

Bayo A., Rodrigo C., Barrado D., Solano E., Allard F., Joergens V., 2013, preprint (arXiv:1312.2739)

Bergfors C. et al., 2013, MNRAS, 428, 182

Birkby J. et al., 2012, MNRAS, 426, 1507

Birkby J. L., de Kok R. J., Brogi M., de Mooij E. J. W., Schwarz H., Albrecht S., Snellen I. A. G., 2013, MNRAS, 436, L35

Blecic J. et al., 2013, ApJ, 779, 5

Bouchy F. et al., 2005, A&A, 444, L15

Bressan A., Marigo P., Girardi L., Salasnich B., Dal Cero C., Rubele S., Nanni A., 2012, MNRAS, 427, 127

Burrows A., Budaj J., Hubeny I., 2008, ApJ, 678, 1436

Cappetta M. et al., 2012, MNRAS, 427, 1877

Casali M. et al., 2007, A&A, 467, 777

Castelli F., Kurucz R. L., 2004, preprint (arXiv:astro-ph/0405087)

Castelli F., Gratton R. G., Kurucz R. L., 1997, A&A, 318, 841

Charbonneau D., Knutson H. A., Barman T., Allen L. E., Mayor M., Megeath S. T., Queloz D., Udry S., 2008, ApJ, 686, 1341

Claret A., Bloemen S., 2011, A&A, 529, A75

Coelho P., Barbuy B., Meléndez J., Schiavon R. P., Castilho B. V., 2005, A&A, 443, 735

Crossfield I. J. M., Barman T., Hansen B. M. S., Tanaka I., Kodama T., 2012, ApJ, 760, 140

de Mooij E. J. W., Snellen I. A. G., 2009, A&A, 493, L35

de Mooij E. J. W., de Kok R. J., Nefs S. V., Snellen I. A. G., 2011, A&A, 528, A49

Dobbs-Dixon I., Lin D. N. C., Mardling R. A., 2004, ApJ, 610, 464

Eggleton P. P., Kiseleva L. G., Hut P., 1998, ApJ, 499, 853

Faber J. A., Rasio F. A., Willems B., 2005, Icarus, 175, 248

Ford E. B., Rasio F. A., 2006, ApJ, 638, L45

Fortney J. J., Lodders K., Marley M. S., Freedman R. S., 2008, ApJ, 678, 1419

Fossati L. et al., 2010, ApJ, 714, L222

Gillon M. et al., 2009, A&A, 496, 259

Gillon M. et al., 2014, A&A, 562, L3

Goldreich P., Soter S., 1966, Icarus, 5, 375

Goulding N. T. et al., 2012, MNRAS, 427, 3358

Gray D. F., 2008, The Observation and Analysis of Stellar Photospheres. Cambridge Univ. Press, Cambridge

Grupp F., 2004, A&A, 420, 289

Gu P.-G., Lin D. N. C., Bodenheimer P. H., 2003, ApJ, 588, 509

Hansen B. M. S., Barman T., 2007, ApJ, 671, 861

Haswell C. A. et al., 2012, ApJ, 760, 79

Hebb L. et al., 2010, ApJ, 708, 224

Hellier C. et al., 2009, Nature, 460, 1098

Hellier C. et al., 2011, ApJ, 730, L31

Hellier C. et al., 2012, MNRAS, 426, 739

Hernández J. et al., 2007, ApJ, 662, 1067

Hodgkin S. T., Irwin M. J., Hewett P. C., Warren S. J., 2009, MNRAS, 394, 675

Hormuth F., 2007, Master's thesis, Univ. Heidelberg

Hormuth F., Hippler S., Brandner W., Wagner K., Henning T., 2008, Proc. SPIE, 7014

Howard A. W. et al., 2012, ApJS, 201, 15

Husnoo N. et al., 2011, MNRAS, 413, 2500

Hut P., 1981, A&A, 99, 126

Irwin M., Lewis J., 2001, New Astron. Rev., 45, 105

Irwin J., Irwin M., Aigrain S., Hodgkin S., Hebb L., Moraux E., 2007, MNRAS, 375, 1449

Jackson B., Greenberg R., Barnes R., 2008, ApJ, 678, 1396

Knutson H. A., Howard A. W., Isaacson H., 2010, ApJ, 720, 1569

Koppenhoefer J. et al., 2013, MNRAS, 435, 3133

Kovács G. et al., 2013, MNRAS, 433, 889

Kupka F., Piskunov N., Ryabchikova T. A., Stempels H. C., Weiss W. W., 1999, A&AS, 138, 119

Lawrence A. et al., 2007, MNRAS, 379, 1599

Leggett S. K., 1992, ApJS, 82, 351

Li S.-L., Miller N., Lin D. N. C., Fortney J. J., 2010, Nature, 463, 1054

Lillo-Box J., Barrado D., Bouy H., 2012, A&A, 546, A10

López-Morales M., Seager S., 2007, ApJ, 667, L191

Maciejewski G. et al., 2013, A&A, 551, A108

Maldonado J., Martínez-Arnáiz R. M., Eiroa C., Montes D., Montesinos B., 2010, A&A, 521, A12

Mamajek E. E., Hillenbrand L. A., 2008, ApJ, 687, 1264

Mandel K., Agol E., 2002, ApJ, 580, L171

Mandushev G. et al., 2005, ApJ, 621, 1061

Mann A. W., Gaidos E., Lépine S., Hilton E. J., 2012, ApJ, 753, 90

Matsumura S., Peale S. J., Rasio F. A., 2010, ApJ, 725, 1995

Maxted P. F. L. et al., 2013, MNRAS, 428, 2645

Meibom S., Mathieu R. D., 2005, ApJ, 620, 970

Mislis D., Hodgkin S., 2012, MNRAS, 422, 1512

Munari U., Sordo R., Castelli F., Zwitter T., 2005, A&A, 442, 1127

Munn J. A. et al., 2004, AJ, 127, 3034

Munn J. A. et al., 2008, AJ, 136, 895

Murgas F., Pallé E., Zapatero Osorio M. R., Nortmann L., Hoyer S., Cabrera-Lavers A., 2014, A&A, 563, A41

Nagasawa M., Ida S., Bessho T., 2008, ApJ, 678, 498

Ogilvie G. I., Lin D. N. C., 2007, ApJ, 661, 1180

Pätzold M., Rauer H., 2002, ApJ, 568, L117

Pavlenko Y. V., 2003, Astron. Rep., 47, 59

Pavlenko Y. V., Jenkins J. S., Jones H. R. A., Ivanyuk O., Pinfield D. J., 2012, MNRAS, 422, 542

Penev K., Sasselov D., 2011, ApJ, 731, 67

Penev K., Jackson B., Spada F., Thom N., 2012, ApJ, 751, 96

Pinsonneault M. H., DePoy D. L., Coffee M., 2001, ApJ, 556, L59

Pont F., Zucker S., Queloz D., 2006, MNRAS, 373, 231

Queloz D. et al., 2001, A&A, 379, 279

Ramsey L. W. et al., 1998, in Stepp L. M., ed., SPIE Conf. Ser. Vol. 3352, Early Performance and Present Status of the Hobby-Eberly Telescope. SPIE, Bellingham, p. 34

Rasio F. A., Ford E. B., 1996, Science, 274, 954

Robin A. C., Reylé C., Derrière S., Picaud S., 2003, A&A, 409, 523

Schlegel D. J., Finkbeiner D. P., Davis M., 1998, ApJ, 500, 525

Schneider J., Dedieu C., Le Sidaner P., Savalle R., Zolotukhin I., 2011, A&A, 532, A79

Seager S., Mallén-Ornelas G., 2003, ApJ, 585, 1038

Sestito P., Randich S., 2005, A&A, 442, 615

Siess L., Dufour E., Forestini M., 2000, A&A, 358, 593

Skrutskie M. F. et al., 2006, AJ, 131, 1163

Snellen I. A. G., Covino E., 2007, MNRAS, 375, 307

Snellen I. A. G. et al., 2009, A&A, 497, 545

Socrates A., Katz B., 2012, preprint (arXiv:1209.5723)

Southworth J., 2008, MNRAS, 386, 1644

Swain M. R., Vasisht G., Tinetti G., Bouwman J., Chen P., Yung Y., Deming D., Deroo P., 2009, ApJ, 690, L114

Torres G., Konacki M., Sasselov D. D., Jha S., 2005, ApJ, 619, 558

Torres G., Fischer D. A., Sozzetti A., Buchhave L. A., Winn J. N., Holman M. J., Carter J. A., 2012, ApJ, 757, 161

Trilling D. E., Benz W., Guillot T., Lunine J. I., Hubbard W. B., Burrows A., 1998, ApJ, 500, 428

Tull R. G., 1998, in D'Odorico S., ed., SPIE Conf. Ser. Vol. 3355, High-Resolution Fiber-Coupled Spectrograph of the Hobby-Eberly Telescope. SPIE, Bellingham, p. 387

van Saders J. L., Pinsonneault M. H., 2012, ApJ, 746, 16

Watson C. A., Marsh T. R., 2010, MNRAS, 405, 2037

Winn J. N., Fabrycky D., Albrecht S., Johnson J. A., 2010, ApJ, 718, L145

Wright E. L. et al., 2010, AJ, 140, 1868

Wright J. T. et al., 2011, PASP, 123, 412

Wyatt M. C., 2008, ARA&A, 46, 339

Yanny B., Guhathakurta P., Bahcall J. N., Schneider D. P., 1994, AJ, 107, 1745

York D. G. et al., 2000, AJ, 120, 1579

Zahn J., 1977, A&A, 57, 383

Zendejas J. et al., 2013, A&A, 560, A92

## SUPPORTING INFORMATION

Additional Supporting Information may be found in the online version of this article:

**Table 1.** The observed WFCAM *J*-band light-curve data for WTS-2 b without correction for dilution.

**Table 3.** The observed INT *i*-band light curve for WTS-2 b without correction for dilution (http://mnras.oxfordjournals.org/lookup/suppl/doi:10.1093/mnras/stu343/-/DC1).

Please note: Oxford University Press are not responsible for the content or functionality of any supporting materials supplied by the authors. Any queries (other than missing material) should be directed to the corresponding author for the article.

This paper has been typeset from a TEX/LATEX file prepared by the author.